# Electromagnetically Actuated Optical Micro-Mechatronic Systems Integrated on PCB

**by**

**Serhan Ömer Işıkman**

**A Thesis Submitted to the**
**Graduate School of Engineering**
**in Partial Fulfillment of the Requirements for**
**the Degree of**

**Master of Science**

**in**

**Electrical and Computer Engineering**

**Koç University**

**July 2008**

Koç University

Graduate School of Sciences and Engineering

This is to certify that I have examined this copy of a master's thesis by

Serhan Ömer Işıkman

and have found that it is complete and satisfactory in all respects,
and that any and all revisions required by the final
examining committee have been made.

Committee Members:

Hakan Urey, Ph. D.

Erdem Alaca, Ph. D.

Arda D. Yalçınkaya, Ph. D.

Date: 09.07.2008

**to Elif…**

## ABSTRACT

In this research FR4, most commonly used printed-circuit-board (PCB) material, is explored for the first time as a new material and integration platform for miniaturized optical, electronic, and mechatronic devices and systems. The results of this investigation have been very fruitful, leading to several novel concepts and intellectual property in this area.

One of the main avenues explored is laser scanning: an FR4 scanner with dynamic focusing feature is designed and demonstrated. Laser scanners are optical devices that manipulate the light beam direction using rotating mirrors or refractive elements, with applications in high resolution display and imaging systems, optical microscopy, barcode reading and laser printing. Dynamic focusing significantly extends the depth-of-focus of laser scanners without compromising the scanner resolution, which cannot be achieved with conventional passive optics. The designed opto-electro-mechanical system comprises a laser diode mounted on a vibrating arm, a rotating platform incorporating a focusing lens, actuators and electronics. The degree of integration demonstrated is not achievable with such ease at low-cost with other technologies. Scan angle greater than 50 degrees and laser plunger deflection greater than 500 μm is achieved at around 50Hz resonant frequency.

One of the major contributions of this thesis is on electromagnetic actuator design and magnetic modeling. Three different types of electromagnetic actuators are analyzed and compared in performance: (i) moving magnet actuators and associated back-emf position sensors, (ii) moving magnetic film actuators, where the developed thin-film magnetic model is valid for non-uniform fields for both saturated and unsaturated material cases and accounts for the magnetic hysteresis using a new closed form analytical expression, (iii) moving coil Lorentz force actuators.

# ÖZET

Bu tez çalışmasında, baskı devre yapımında kullanılan en yaygın malzeme olan FR4, ilk kez minyatür ve tümleşik bir optik, elektronik ve mekatronik sistem platformu olarak kullanılmaktadır. Bu alandaki araştırmalar oldukça verimli olmuş, çok sayıda yenilikçi tasarım ve fikri mülkiyet hakkının ortaya çıkmasına öncülük etmiştir.

FR4 ile çalışılan araştırma konularının başında lazer tarayıcılar gelmektedir. Bu kapsamda, dinamik odaklama özelliğine sahip bir FR4 tarayıcı tasarlanmış ve üretilmiştir. Lazer tarayıcılar, döner ayna ya da ışığı kıran elemanlar kullanarak ışık ışınlarını yönlendirebilen optik aygıtlardır. Tarayıcıların başlıca uygulamaları arasında yüksek çözünürlüklü görüntüleme, optik mikroskopi, barkod okuma ve lazer yazma yer almaktadır. Dinamik odaklama özelliği, pasif optik elemanlar ile başarılamayan bir şekilde, çözünürlükten kayıp vermeden odak genliğini genişleterek tarayıcının çalışma menzilini yüksek oranda artırır. Tasarlanan opto-elektro-mekanik platformda, tümleşik hareketli bir kola yerleştirilmiş lazer diyot, odaklama lensi, elektronik elemanlar, tahrikleme elemanları ve tüm bu parçalar ile bütünleşik dönebilen bir tarama platformu bulunmaktadır. Böylece, diğer teknolojiler ile başarılması çok güç bir bütünleştirme (entegrasyon) seviyesine ulaşılmıştır. 50 dereceden fazla tarama açısı ve 500 mikrondan fazla lazer diyot kolu deplasmanı, 50Hz civarında doğal frekanslarda elde edilmiştir.

Bu çalışmanın önemli başarımlarından biri de elektromanyetik tahrikli sistem tasarlanması ve modellenmesidir. Üç farklı tahrik mekanizması ile çalışan tarayıcılar modellenmiş ve analiz edilmiştir: (i) hareketli mıknatıs mekanizması ve pozisyon geri beslemesi veren bütünleşik ters elektro-motif kuvvet (back emf) voltajı algılayıcısı, (ii) hareketli manyetik film tahrikli sistemler ve eşdeğerli olmayan manyetik alanda, doygunluğa ulaşmış ve ulaşmamış filmler için geçerli olan, ardıl izlemi (hysteresis) yeni bir fonksiyon kullanarak kapsayan manyetik ince film modeli, (iii) Lorentz kuvveti ile çalışan hareketli bobin sistemleri.

## ACKNOWLEDGEMENT

Foremost, I would like to express my utmost gratitude to my thesis advisor Prof. Hakan Urey for providing his invaluable support and brilliant ideas throughout my research. His continuous encouragement and trust on me made all the hard work so easy, productive and fun. Spending more than six years in the Optical Microsystems Laboratory (OML), where I entered as a freshman and graduated as a master's degree researcher, has truly been a great opportunity.

I was really fortunate to have the opportunity to work with Randy Sprague from Microvision Inc., our project partner company in USA. I have learned so much from him during our weekly project discussions. With his expertise and bright ideas, his engineering perspective has been extremely valuable and inspiring. I would like to sincerely thank Microvision for their financial support in the project.

I would like to sincerely thank Prof. Arda Yalçınkaya, who has made significant contributions to the research presented in this work, and Prof. Erdem Alaca for kindly taking part in my thesis committee and providing their invaluable insight.

I acknowledge TUBITAK for granting the graduate student fellowship for my master's degree studies and supporting me to attend international conferences.

I would like to thank my dear colleagues, all the past and present members of OML for making the long hours spent in the lab so fun. It was encouraging to see that one friend was always in the lab working at any time of the day. I had the privilege to work with Çağlar Ataman, the legendary member of OML, who was always willing to help and teach. Special thanks to M. Fatih Toy, the troubleshooter of OML, for solving any kind of experimental problems and providing inspiring ideas. Many thanks to Sven for his invaluable help with experiments and instrumentation. I would like to thank Onur for

providing his insight and practical approach whenever I needed. Those years spent in OML will always remain memorable.

I would like to thank my mom, dad and brother for their endless support. It was always reassuring to know that they were there to help me.

Last, but definitely not the least, I would like to thank Elif. There are so many reasons to thank you that I will not even attempt to list one. This work would not be possible at all in your absence.

## LIST OF FIGURES

## LIST OF TABLES

## TABLE OF CONTENTS

# 1 INTRODUCTION

Laser scanners are at the heart of many optical applications today. A simple laser scanner is a rotating mirror or an active refractive element, which allows manipulating light by scanning, steering or modulating light beams. Most common applications of laser scanners are high resolution display and imaging, switches for optical communication and optical microscopy. A short discussion on different scanners and their applications of scanners is given below.

## 1.1 Applications of Scanners

### *1.1.1 Barcode Reading Applications*

A barcode is a symbology with encoded information that can be extracted by a decoding machine. The decoding device is called a barcode reader. A simple schematic of a scanning based barcode reader is shown in Figure 1-1.

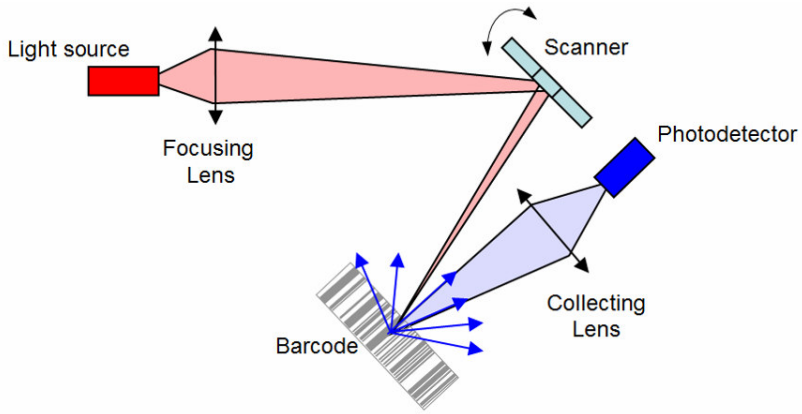


Figure 1-1 A typical barcode reader setup

In a scanning based barcode reader, the symbology is illuminated with a focused light beam. The focused spot is scanned on the barcode to “look at” each point of the barcode pattern. The reflected light is collected on a photodetector, where the optical signals are converted to electrical signals. If the focused spot is reflected from a white zone of the barcode, photodetector receives high optical power whereas a reflection from a black zone results in almost zero optical power reflection. Therefore, the electrical output of the photodetector is modulated by the scanned barcode pattern. After this stage, the electrical signal received after a full scan of the barcode is interpreted by the electronics circuitry to decode the information in the symbology.

A barcode reader requires a scanner, which can rotate at large angles at low frequencies. (<100 Hz) The large angle requirement becomes critical for reading barcodes from close distances so that the scan line created by the scanner is long enough to span the whole barcode pattern. Low frequency scanning is required to keep the bandwidth of the decoding electronics as low as possible. Increasing the bandwidth of the electronics also increases cost, which is not desired for commercial reasons. Therefore, barcode readers mostly employ low-cost scanners driven by electrical motors at low frequencies.

Polygonal scanners have been successfully used in barcode readers. A polygon scanner is simply a rotating mirror, with reflective faceted surfaces. These mirrors are rotated by electrical motors to scan the incident light beam. As shown in Figure 1-2, polygon scanners are rigid structures with good mechanical reliability. These scanners are typically manufactured from aluminum or nickel, which makes the production cheaper. Therefore, in terms of cost and reliability, polygon mirrors are ideal for use in barcode readers.

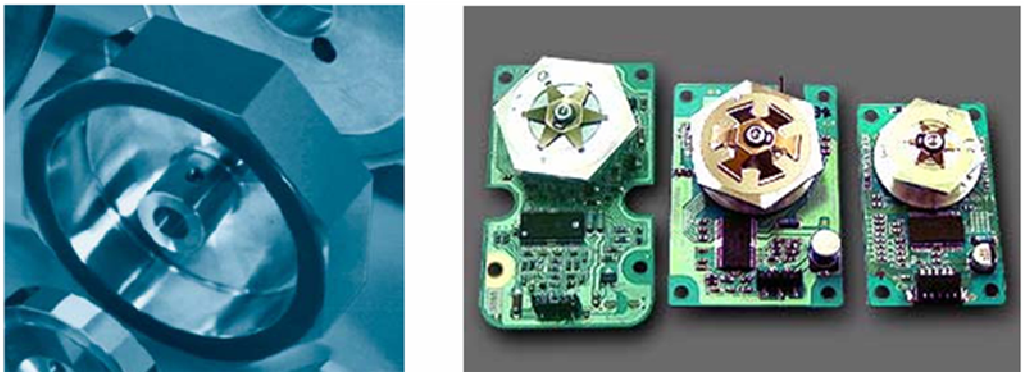

Figure 1-2 A polygonal mirror (left) and a polygon scanners driven by brushless motors (photo courtesy of Lincoln Laser Corp.) (right)

Galvanometer based scanners are also being used in scanning based barcode reading applications. A galvanometric scanner, or a *galvo*, is basically a galvanometer [1] loaded by a mirror, which is rotated by the rotor to scan the light beam. Figure 1-3 shows a basic galvanometer where the coil is the rotor and the magnet is the stator (left) and also several commercial galvanometric scanners. (right)

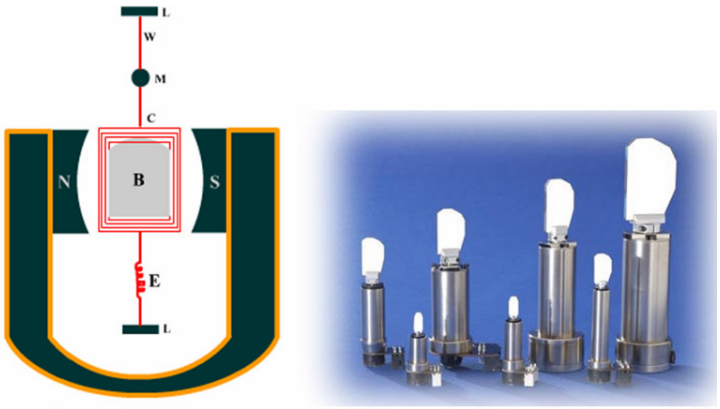


Figure 1-3 The schematic of a typical galvanometer (left) and commercially available galvanomteric scanners (photo courtesy of Cambridge Technology Inc.) (right)

Despite their scanning performance, galvanometric and polygonal scanners cannot meet the increasing demands towards miniaturization. Additionally, discrete components cannot be integrated on such scanners. Light sources, detectors, position feedback elements and electronics have to be separate stages mounted on separate locations in the barcode reader. Therefore, galvos or polygon scanners cannot be used as highly-integrated scan engine platforms where optoelectronics, mechanics and electrical components are merged on the same platform. This stands as a limit to use these scanners in miniaturized systems.

### *1.1.2 High Resolution Display Applications*

2D micro-scanners scan the screen in a raster fashion and with proper modulation of light, an image can be displayed. By refreshing the image on the screen, video display can be performed.

Scanners produced by micro-technology have proven very successful for display and imaging applications. Two-dimensional scanners, which can steer a light beam both horizontally and vertically, are used for high resolution display applications. Figure 1-4 shows a 2D MEMS scanner with gimbal structure and a sample raster scan pattern produced by such scanners. Microvision Inc., USA has successfully used this principle to produce a see-through head mounted retinal scanner display device, which scans a light beam onto the user's retina to display the video content. [2] Figure 1-5 shows the optical system employed in the retinal scanner display.

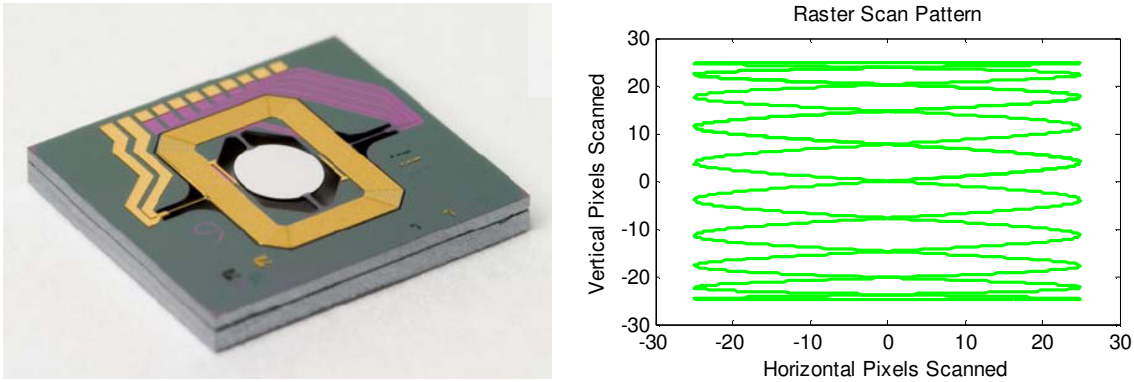


Figure 1-4 (a) A 2D MEMS scanner produced by Microvision Inc. (photo courtesy of Microvision) (b) An exemplary 2D raster scan pattern.

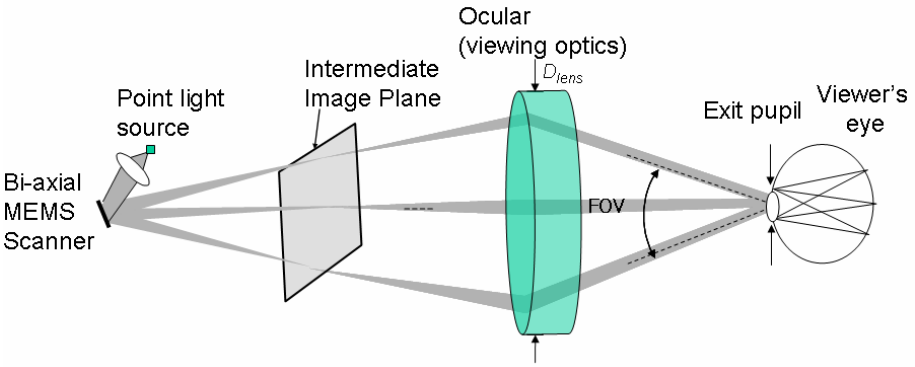


Figure 1-5 An illustration of the Retinal Scanner Display product of Microvision Inc., USA employing a MEMS scanner. [2]

### *1.1.3 Switches for Optical Communications*

An optical switch is a component that selectively directs the optical signal in a channel of a fiber network or optical integrated circuit to another channel in the path. Before the use of optical MEMS components, this switching mechanism required

conversion to electrical domain, significantly increasing switching time. However, the use of optical switches, which are basically arrays of micro-scanners sending a light signal in a channel to another one, enables routing an optical signal in a network without domain conversion of energy. MEMS scanners have successfully been implemented in optical networks for this purpose. [3][4] Figure 1-6 shows both a digital and analog array of MEMS optical switch configurations to be used in optical communications systems.

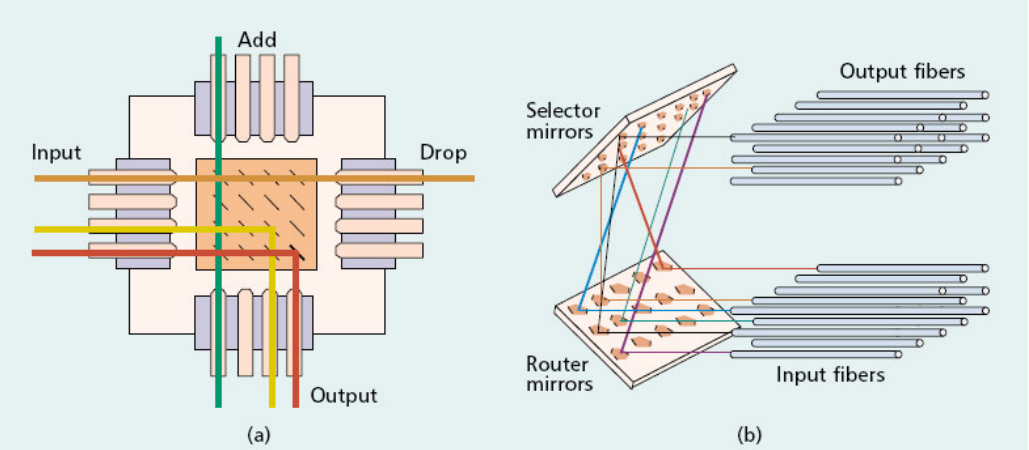


Figure 1-6 (a) Shows an array of digital MEMS mirrors for optical switching (b) array of analog optical switches for switching (figure taken from [3] )

### *1.1.4 Applications in Medical Imaging*

An important medical imaging technique where scanners are employed is confocal optical microscopy. This is a high-resolution imaging technique, which allows layer-by-layer 3D imaging (optical sectioning) of thick specimen. The key idea behind this technique is to illuminate the specimen with a focused spot and collect only the scattered light which is imaged on a pinhole in front of the detector. [5][6] As shown in Figure 1-4,

the collected light from the scanned specimen is imaged on a confocal pinhole and most of the collected light which is out-of-focus on the pinhole plane is rejected, substantially increasing the resolution. Scanners are at the heart of confocal laser scanning microscopy. Olympus has realized a microscopy system employing two MEMS scanners, one for horizontal and one for vertical axis scanning of the specimen. [5]

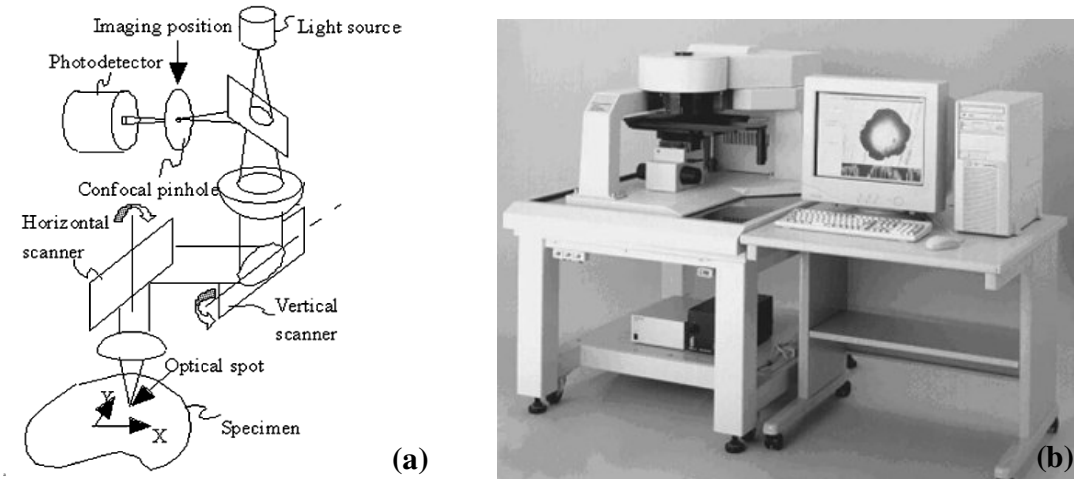


Figure 1-7 (a) Shows a schematic of a typical confocal laser scanning microscope (b) Olympus OLS1100 Microscope system employing two electromagnetic MEMS scanners (figure taken from [5] )

Another important medical imaging technique is optical coherence tomography (OCT), which allows high resolution *in vivo* cross-sectional imaging of tissues. Its basic principle relies on white light interferometry. A broadband light source is split into two arms, one being the reference arm and the other scanning the specimen. The reflected light is then interfered with the reference beam. Due to low coherence length of the input light source, maximum interference amplitude is achieved at zero optical path difference achieved by translating the reference mirror, whose position feedback provides information

about the location of the sample under the microscope. [7][8] An OCT system similar to the one illustrated in Figure 1-8 requires one out-of-plane translating actuator for modulating the path difference in reference arm and also a second scanning optics to scan the surface of interest. Therefore, OCT is one of the most important medical imaging techniques requiring the use of scanners.

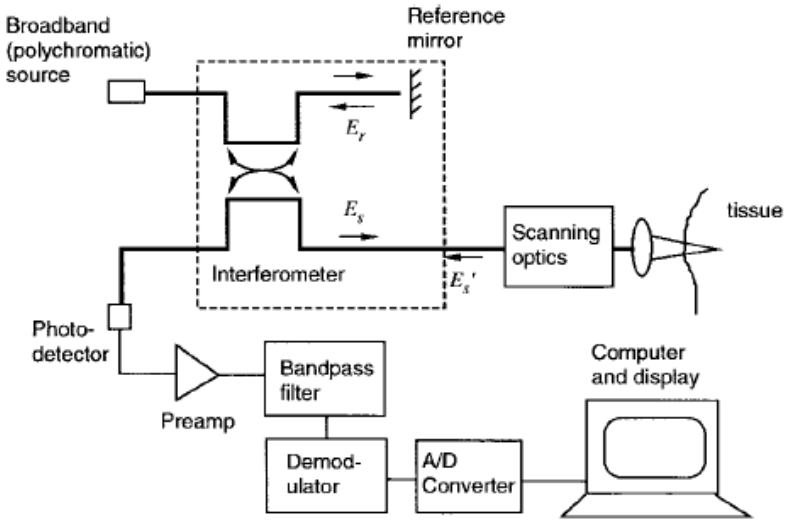


Figure 1-8 Shows the component blocks of an OCT imaging system (figure taken from [8] )

## 1.2 Contributions of the Thesis

A novel scanner platform, electromagnetic actuation method, and optical integration architecture are developed in this thesis, which offer key advantages in various scanned beam display and imaging applications. The platform technology developed is based on FR4 that stands for *Flame Retardant Type 4* fiber-glass epoxy composite substrate and is the most commonly used substrate in standard printed circuit boards (PCBs) today. [9][10]

The main contributions of the work presented in this thesis are summarized below.

- *Presenting FR4 as a New Opto-Electro-Mechanical System Platform:* FR4 is proposed as a new platform for actuated opto-electro-mechanical system design. FR4 technology is more attractive than using MEMS or other conventional scanners for certain applications. The main advantage of FR4 becomes apparent for low frequency and large deflection applications (discussed in more detail in Chapter 2). Furthermore, a high-end FR4 scanner with extended depth of focus an integrated optics is realized and presented in Chapter 5. A journal article is submitted to *Photonics Technology Letters* [38] and another journal article to *Sensors and Actuators* is in preparation. [27]

- *Magnetic Anisotropy Torque Calculation for Multi-domain Materials in Non-uniform Fields:* As discussed in section 1.2, one of the actuation methods for electro-magnetic FR4 scanners is the soft magnetic film actuation. Most of the time, the soft magnet plated area has dimensions that are comparable to the footprint of the drive coil. Therefore, the magnetic field distribution on the magnetic film is not uniform. In this case, if the field strength is not sufficient to saturate the soft magnetic film, the magnetic material cannot be considered as single domain. In this thesis, a new technique to calculate the total force and torque on the magnetic film is presented in section 4.1.2, which is not restricted to uniform magnetic fields or saturated magnetic materials. An article discussing the newly developed magnetic model for force and torque computation in static field and 2D scanning was published in *Journal of Selected Topics in Quantum Electronics* [21]. Another article discussing the dynamic actuation of thin films was submitted to *IEEE Transactions on Magnetics* [23]

- *Simple Magnetic Hysteresis Modeling Function for Dynamic Actuation:* For dynamic deflections of soft magnetic film actuated scanners, magnetic field is alternating. Therefore, the B-H loop of the magnetic material is traced at each cycle of the alternating field. For small deflection cases under low magnetic field strength, the effects of magnetic hysteresis become visible. In this work, a new closed form analytical expression is proposed in section 4.1.3 to easily model the BH-loop of ferromagnetic films, which allows accurate modeling of soft magnetic film actuated scanners. The magnetic film modeling effort presented in this work is done with millimeter size FR4 scanners. However, the methods described are valid for micro-scanners, as well. The article submitted to *IEEE Transactions on Magnetics* discusses the BH-loop model [23]

- *Dynamic Focus FR4 Scanner:* A novel torsional FR4 scanner with dynamic focusing is designed, manufactured and characterized as discussed in chapter 5. For conventional optical scanners, the depth of field of the focusing optics is limited by the *Rayleigh range* of the laser beam. Dynamic focusing feature is integrated in FR4 scanners to extend the working range of the device to scan surfaces with focused spot for a longer depth range. The *Phot. Tech. Lett.* article in review discuss the dynamic focusing features. [38]

- This work led to four US patent applications that are filed by Microvision Inc. (USA) with the author of this thesis as co-inventor, and a product development effort for an advanced barcode reader jointly with Microvision Inc. (USA) and a high-volume manufacturing company in India.

# 2 FR4 AS A NEW INTEGRATED OPTO-ELECTRO-MECHANICAL SYSTEM PLATFORM

Using a polymer called FR4 as an opto-mechanical-system platform is one of the main novelties of the research presented in this thesis. FR4 stands for *Flame Retardant Type 4,* and it is the most commonly used substrate in standard printed circuit boards (PCBs) today. In this thesis, FR4 is being proposed as a new platform for actuated opto-mechanical systems. [9][10]

In Optical Microsystems Laboratory at Koc University, several projects utilizing FR4 as an integrated opto-electro-mechanical platform are being conducted. Although this thesis presents the research on torsional scanner for imaging applications in the following chapters, FR4 scanners are being employed in 3D display and Fourier transform spectrometer systems.

## 2.1 Highlights of FR4 Material and FR4 Scanner Technology

FR4 is a dielectric laminate epoxy resin combined with a glass fabric substrate. It is a generic name given to materials meeting the requirements of *Underwriters Laboratories UL94-V0* [11]. It is the main structural material used in making PCBs. Therefore, FR4 is a well engineered reliable material with superior electrical, mechanical and thermal stability so that it can be used in different environments, from military and space applications to high-end electronics devices.

The reliability of FR4 polymer makes it very suitable to be used as an electro-mechanical platform. Using standard PCB technology, any desired shape can be carved from a sheet of FR4. Features <500μm wide can be easily cut from FR4 with about 50μm tolerance. The incorporation of laser cutting increases the cutting resolution and the trend is toward further reducing the tolerances. Therefore, millimeter sized actuators can easily be produced by conventional PCB technology.

Copper layers come readily available on FR4 sheets. Together with the fine PCB cutting, this makes FR4 ideal to be used as an electro-mechanical platform. Today's technology allows etching the copper on FR4 to produce copper feature sizes as small as 100μm with standard routing process and lower resolutions are possible with laser writing lithographic techniques. Therefore, surface mount electronics components can be mounted on the actuator itself and all the required electrical connections of the polymer actuator can be routed on the actuated device, without requiring wire-bonding or break-outs.

The electrical connections on the FR4 platform can also be used for electro-magnetic actuation as well as signal routing of electronics components. The copper on the FR4 can be etched as a planar coil to actuate the device with an external magnet. A very simple torsional FR4 scanner with a rotating planar coil is shown in Figure 2-1. An aluminum coated silicon mirror (not shown in the figure) is bonded on the central square platform for laser scanning.

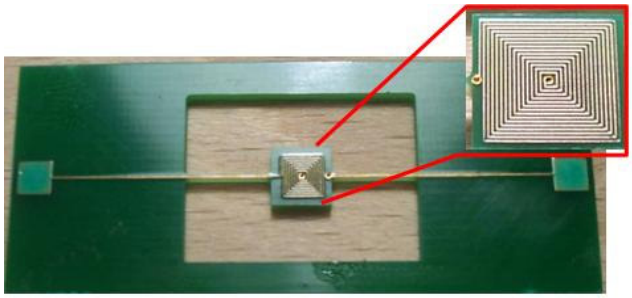

Figure 2-1 A simple torsional FR4 scanner with a routed planar coil produced from a sheet of FR4 using conventional PCB technology

As mentioned above, many different scanner designs with different gimbal structures can be envisioned and easily produced with this technology. Figure 2-2 shows seven different scanner types with different flexure designs. All the scanners are produced on the same double sided copper laminate PCB board, which has dimensions of 20cm x 15cm. Each scanner is connected to the main board with four break-out tabs for easy detaching.

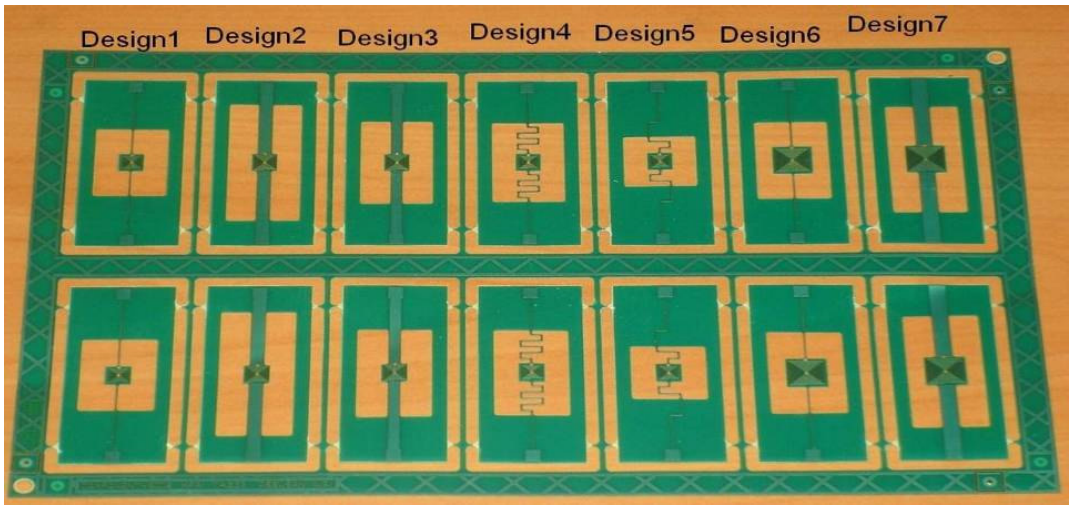


Figure 2-2 Shows seven different FR4 scanner designs produced on the same FR4 sheet. The FR4 sheet has dimensions of 20cm x 15cm

The actuation of FR4 scanners can be achieved by soft magnetic film electroplating, as well. In this type, the copper layer on the central square platform of the scanners is not etched, but used as a seed layer for permalloy (Ni-Fe alloy) plating. Using an external coil or magnet, the scanner can be actuated both with DC and AC forces, resulting from the magnetization of the ferromagnetic permalloy layer. Two different FR4 scanners with cantilever and torsional geometries are shown in Figure 2-3.

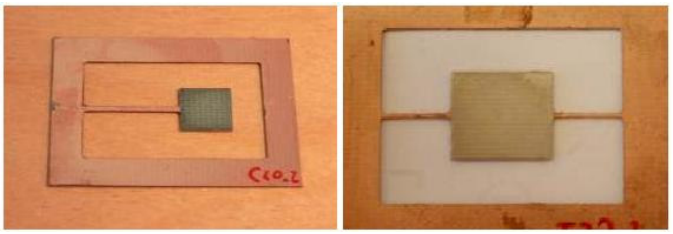

Figure 2-3 Shows two different FR4 scanner designs with electroplated permalloy for magnetic actuation. [14]

Similar to soft magnetic film actuation, permanent magnets with appropriate polarization direction can also be mounted on FR4 scanners to be actuated with external electro-coils. As expected, this approach enables larger force generation compared to magnetic films, but reduces the natural frequency of the desired mode due to added mass and inertia.

The reader is referred to the section 4 of the thesis for detailed analysis and discussion of various types of electro-magnetic actuation of FR4 scanners.

The most relevant material properties of FR4 used for mechanical design is summarized in Table 2-1. Note that FR4 is not a single material but a family of materials meeting certain specifications. Therefore, these values may vary for FR4 sheets from different vendors.

| Parameter | Value |
|---|---|
| **Young's Modulus [Pa]** | $15 \times 10^9$ |
| **Torsional Modulus [Pa]** | $6.5 \times 10^9$ |
| **Poisson's Ratio** | 0.2 |
| **Density [kg/m$^3$]** | 1900 |

Table 2-1 Summarizes the most commonly used material properties for mechanical design of FR4 actuators.

FR4 is a promising platform that lends itself to high degree of integration with electrical, mechanical, optical and magnetic components. In this perspective, depending on the application, FR4 technology becomes more attractive than using MEMS or other conventional scanners for certain applications. The main advantage of FR4 becomes apparent for low frequency and large deflection applications. FR4 scanners are ideal for rotating large masses with large deflections at low frequencies thanks to their compliant structure, high flexibility and high stress limit relative to their size. This allows mounting optical components like lenses and mirrors using opto-mechanical elements on the FR4 platform. Additionally, die level components like laser diodes and photo-detectors can be placed and wire-bonded to the electrical connections on FR4. Permanent magnets with relatively large masses can be mounted on the scanners for large deflection applications and the scanner platform operates reliably without showing significant performance degradation and fatigue as discussed in section 2.3. [10]

## 2.2 Production of FR4 Sheets with Copper Laminates

A printed circuit board sheet is composed of two main layers, which are the insulator substrate and the copper foils covering the top and bottom layers of the insulator. Copper is

chosen for two main reasons: it is cost-effective and a good conductor. Therefore, in all PCBs, the conductive layer is copper. On the other hand, there is a wide selection available for the insulator substrates, with different material properties.

The main requirements for the insulator layer is that it should be strong to support components and withstand shocks; it should be able to dissipate heat since certain electrical components require high powers; it should have a low coefficient of thermal expansion; it should be chemically resistant; it should not absorb excessive moisture and not be flammable.

Typically, the insulator substrate consists of a resin material (mostly epoxy) and inorganic reinforcement materials, such as random glass fibers, woven glass fibers, paper cloth, metal cores and graphite fibers. Figure 2-4 shows an SEM cross-section image of a woven glass fiber from an FR4 sheet. The woven reinforcement fibers are dipped into the resin and then squeeze-rolling is applied to form laminates. Copper and insulator layers are pressed under high pressure and temperature (about 150°C) between steel plates. In this process, the resin flows and cures immediately, forming a strong sheet. [12] A microscope image of a multilayer FR4 is shown in Figure 2-5.

Considering the main aspects of the substrate layer of a PCB listed above, FR4 has become widely popular for its excellent material properties and reliability. Like most PCB substrates, FR4 is composed of epoxy and woven glass fibers, with fill and grain directions. (or weft and warp). A sheet of FR4 is made up of laminates, where layers are bonded by prepreg layers. Depending on FR4 thickness, which can vary from 100μm up to a few millimeters, the number of layers changes.

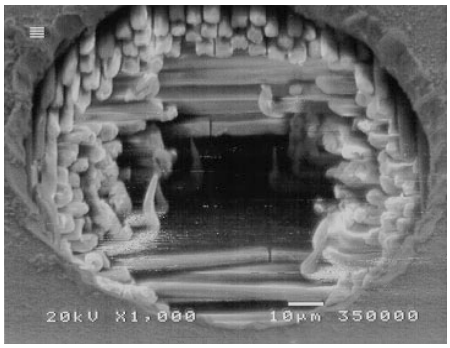


Figure 2-4 SEM cross-section image of a glass fiber cloth used in FR4 material [13]

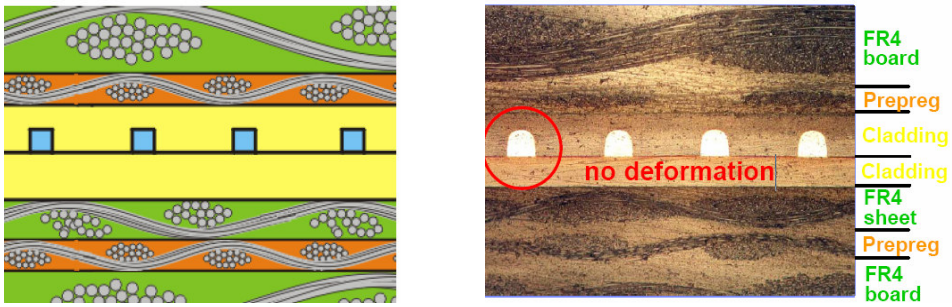


Figure 2-5 The laminated structure of FR4 (left) and a microscope cross-section image of a multilayer PCB board with optical waveguides sandwiched between layers (photo courtesy of IBM, Zurich)

## 2.3 Comparison of FR4 Platform to MEMS Technology

Along with the developments in micro-technology, there has been an increasing trend in engineering to make things smaller. Although this trend is driven by the need for miniaturization, the way to make things smaller does not always require micro-fabrication. For certain applications, there is a clear need for a new platform to balance the miniaturization and other performance parameters. FR4 is an ideal material to fill in this

gap. It still allows production of millimeter sized devices together with offering other advantages. Below is a comparison of FR4 and MEMS platforms with respect to the main figures of merit for a scan engine.

*Degree of integration:* Silicon technology is proven to be a good platform for integrating electronics with electro-mechanical components, as exemplified by Digital Micromirror Device (DMD) technology [14] and resonant gate transistors [16]. However, integration of micro-mechanics with optoelectronic components such as lasers and photodiodes is much harder and the author is not aware of demonstration of such integration, mainly due to fabrication process and interconnect difficulties. Most MEMS scan engines realized up to date are only composed of the vibrating scan mirror. Nevertheless, scanning element is only one component of a more complicated photonic module. At the minimum, a scan engine has a second major part, which is the collecting optics and a third part, which is basically the signal processing electronics. Therefore, simply replacing the scanner with a MEMS based one is not a major improvement for most systems. [17] Due to the constraints in micro-fabrication technology, large components like lenses, opto-mechanics or magnets are much more difficult to mount on the scanner itself. Furthermore, the scanner size needs to grow to accommodate those components to allow high degree of integration. However, the cost of such a system would increase significantly with the increasing silicon area. On the other hand, FR4 technology allows for integration of any component on the scanning platform without increasing the costs. On an advanced FR4 scan engine, the focusing optics can be mounted on the scanner as well as the collection optics, which is needed for more efficient light collection with rejected ambient light. Furthermore, permanent magnets or coils can be bonded on FR4 for electromagnetic actuation. The signal processing circuitry can also be integrated on the device itself using PCB technology. A collection of different FR4 scanner prototypes integrated with various components are shown in Figure 2-6 to illustrate the wide range of integration possibilities

for FR4 technology. The availability of multilayer PCBs further increases the space to use for more complicated routing. Adding those components decreases the resonant frequency of the scanners, which are already made of a soft polymer compared to silicon. Therefore, for low frequency applications, FR4 becomes more attractive compared to silicon.

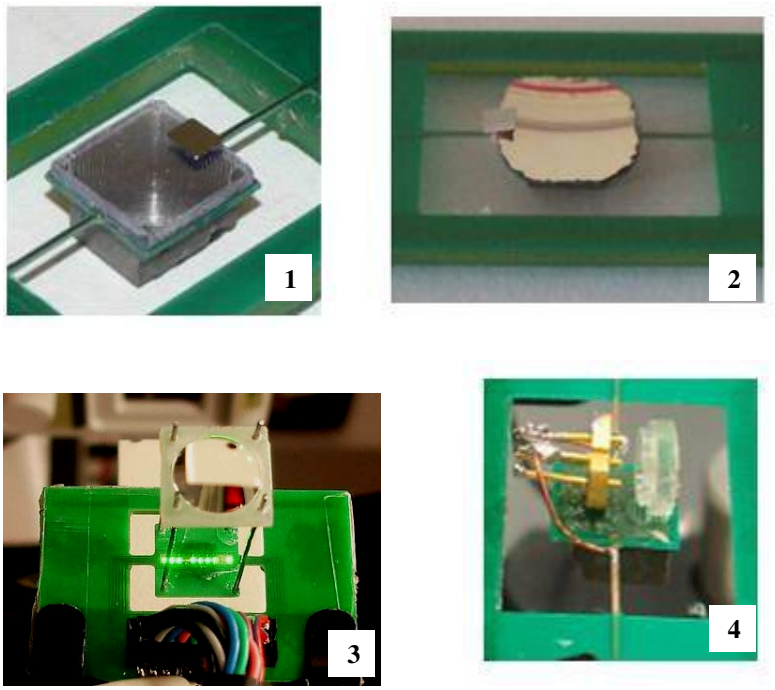


Figure 2-6 Shows various FR4 scanners integrated with optical components. Fresnel mirrors (1), curved mirrors (2), LED arrays (3), lens-laser diode assemblies (4) can easily be integrated on FR4

Position sensing components are needed for high-precision closed-loop control of scanners. While Silicon MEMS scanner can have optical, electro-static, or piezo-resistive angle sensors that require additional process or system complexity, routing a coil around the fixed frame of the FR4 provides a simple back-emf angle or deflection sensor at no additional cost. This option further increases the degree of integration for an FR4 scanner.

*Scanning Frequency:* For many scanning applications, high frequency operation of silicon scanners is undesired, since it makes the electronic processing harder and more expensive due to electronics bandwidth requirements. For example, for bar code reading, scan rates are required to be below 100Hz, which is difficult to achieve with Silicon microscanners. However, FR4 scanners can easily be designed for low frequencies and still be reliable and robust. However, for high frequency scanning, FR4 loses its advantage since it cannot scan with large angles at high frequencies due to increased stiffness of flexures. Therefore, as resonant frequency is increased, much more power is required to get to the same deflection angle.

*System size:* In terms of overall size, MEMS devices are much smaller than FR4 based systems. This makes MEMS platform more feasible for applications like body implants or endoscopy. In this sense, FR4 actuators are not expected to replace their MEMS based counterparts where volume should be kept as small as possible. However, most of the time, device performance specifications like power consumption, light collection efficiency and scanning performance are critical specifications of a device and an optimization of all these parameters is required rather than only concentrating on making the structure as small as possible. In such applications, FR4 can allow for designing systems that are still reasonably small, but are better in terms of other aspects of the scan engine.

*Reliability:* One of strongest aspects of MEMS scanners is that they are reliable for long term operation. Silicon is a brittle material, which is intact as long as it does not break. Having a high flexural stress limit, silicon micro-scanners are very reliable for long run operation. FR4 scanners have a much lower flexural stress limit. However, due to relatively large geometry and low Young's modulus of FR4 scanners, stress concentration in the flexures does not exceed the maximum limits even at large deflections. The accelerated lifetime tests performed on FR4 scanners reveal that no significant performance decrease is

observed even after several hundred millions of cycles of operation. It is observed that the resonant frequency of FR4 scanners drop less than 1% after long run tests performed at 20° total optical scan angle. [10] Hence, FR4 is a reliable platform for actuated opto-electro-mechanical system design. Figure 2-7 shows the results of long run tests performed on moving magnet type FR4 scanners. The scanner is driven at resonance, 546 Hz; the resonant frequency, quality factor and total optical scan angle (TOSA) are monitored. As the figures show, the scanner operation is stable and reliable even after 300 million cycles. No significant change in any of the monitored parameters is observed, which shows that plastic deformation and fatigue has not occurred during the reliability tests.

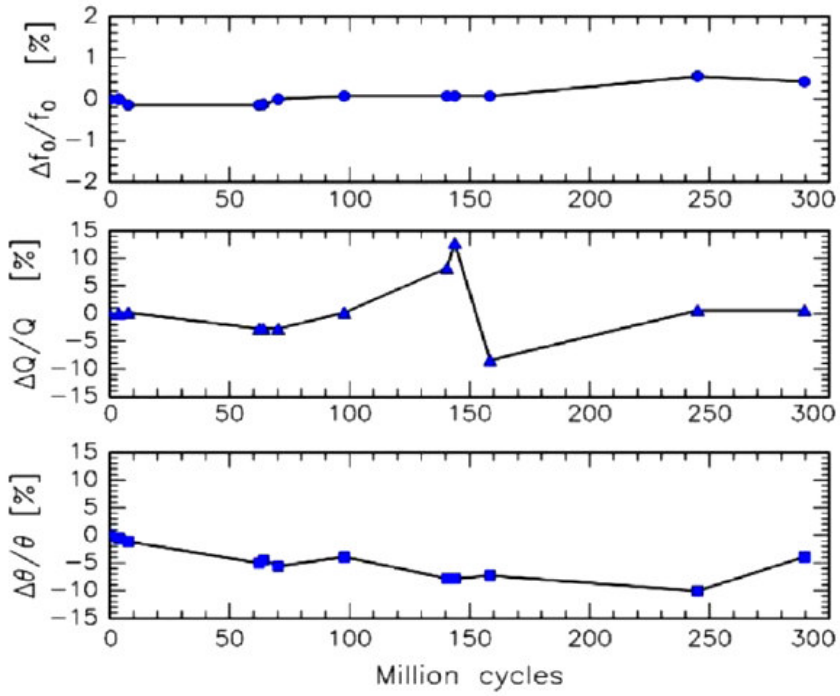


Figure 2-7 Long run test result with a moving coil type FR4 scanner. Resonant frequency, quality factor and scan angle is monitored during reliability tests.

FR4 scanners have also been tested for high temperature durability. For this test, a scanning system is placed in a temperature controlled hood. The quality factor and resonant frequency of the FR4 scanner is monitored during operation. The temperature is increased up to 90° and then decreased back to room temperature. After this temperature cycle, FR4 scanner is observed to recover its original Q and resonant frequency characteristics. This test reveals the material reliability of FR4 in terms of thermal durability. However, it is important to note that the Q factor drops drastically at high temperatures. This is due to the fact that the polymer resin in FR4 becomes softer when heated, which increases the structural damping and loss.

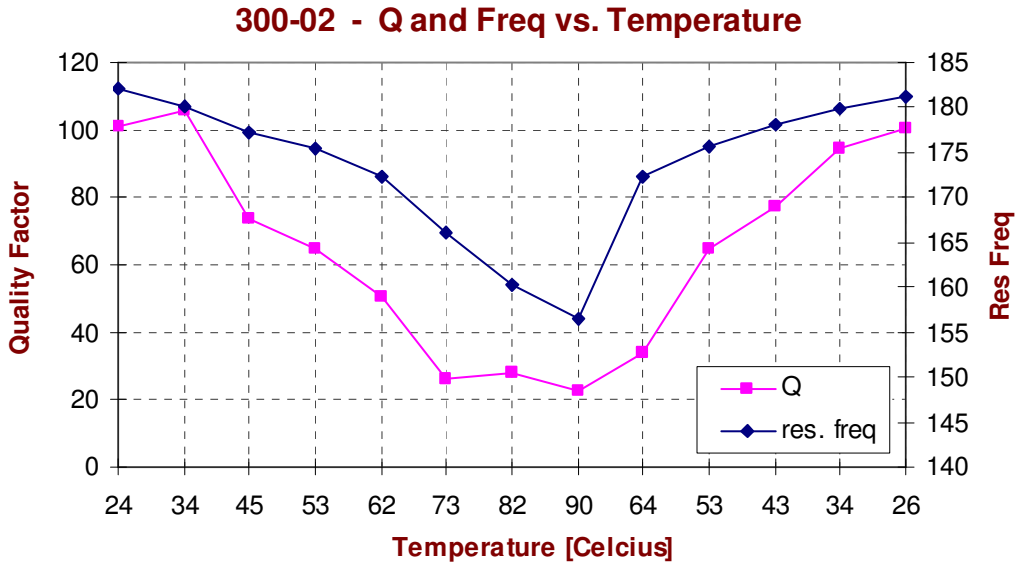


Figure 2-8 Quality factor and resonant frequency changes for an FR4 scanner in high temperature test

*Commercialization:* Production costs are very critical to allow a system to achieve commercial success. The main claim of the MEMS technology is that micro-technology actually allows cheap production if a device is to be mass produced. Although it is expensive to make a master, replication is low-cost and mass production makes MEMS devices feasible. However, the amount of replicas is not the only driver for the cost. Process development, fabrication cycle-time, and engineering skills required during the development phase is also critical. MEMS design forces the designers to make as many mistakes as possible in parallel due to long-lead-time and costly fabrication cycles. FR4 offers a great advantage in this sense since it is much easier and faster to make millimeter size PCBs and integrate it with other components rather than micro-fabricating an integrated MEMS platform. The fact that standard and well developed PCB technology is mostly sufficient for FR4 technology makes it a good candidate for commercial success.

Table 2-2 provides a summary comparing FR4 and MEMS platforms with respect to some relevant parameters required for system design. The comparison in this table is mostly about the material properties and production specifications available in today's technology.

| | FR4 | Silicon |
|---|---|---|
| Fabrication | Standard PCB | MEMS |
| Density [kg/m$^3$] | 1900 | 2300 |
| Density of Copper [kg/m$^3$] | 8960 | 8960 |
| Young's Modulus [GPa] | 15 | 168 |
| Torsional Modulus [GPa] | 6.5 | 51 |
| Flexural Stress Limit | 50 MPa | 1 GPa |
| Min. Coil Trace Width | 100um | 10-70um |
| Min. Coil Line Spacing | 100 um | 10um |
| Min. Via Hole Size | <25um (laser cutting) | very difficult |
| Min. feature size | <100um (laser cutting) | 2um (lithography) |
| Copper thickness | 30um | 10um |
| Number of Coil layers | 2 - 10 | 1 |
| Coil Resistance | Low | High (typical) |
| Copper thickness | 30um | 10um |
| Number of copper layers | 10 | 2 |

Table 2-2 Comparison of FR4 and MEMS technology as a scanner platform

# 3 MECHANICS OF TORSIONAL SCANNERS

In this chapter, mechanics of scanners is studied. Although many different scanner designs can be envisioned, mechanics of cantilever beam and torsional scanners is investigated. Section 3.1 shows how to calculate the equation of motion of a torsional scanner using Euler-Lagrange equation. The analytical results are compared with finite element analysis (FEA) results. FEA is performed using *Comsol Multiphysics 3.3* ®.

## 3.1 Analytical Modeling

The equation of motion (EOM) of a scanner is needed to fully investigate its vibration under external force and torque. Euler-Lagrange equation can be utilized to find the EOM of a torsional scanner. The scanner of interest is basically a rectangular scanning frame, suspended by two flexures, similar to the right hand picture in Figure 2-3. The total kinetic and potential energy of the scanner is needed for this calculation. The kinetic energy, $E_k$ is basically the energy of the moving mass of the scanner and the potential energy, $E_p$ is the energy stored in the springs, namely the flexures. Knowing the kinetic and potential energies, the EOM can be calculated as given by (3-1) and (3-2): [18]

$$L = E_k - E_p \tag{3-1}$$

$$\dot{\theta}\frac{\partial L}{\partial \dot{\theta}} - \frac{\partial L}{\partial \theta} = T_{mag} \tag{3-2}$$

Since the velocity of each point on the scanner is different, the kinetic energies of each infinitesimal volume on the scanner paddle are different. In order to account for that, the scanner frame is divided into slits along the dimension normal to the flexures ($L_m$) with uniform volumes to calculate the total kinetic energy as shown in Figure 3-1. The kinetic

energy of the flexures can be neglected since their mass is negligible and velocity is almost zero along the flexures due to being on the torsional rotation axis.

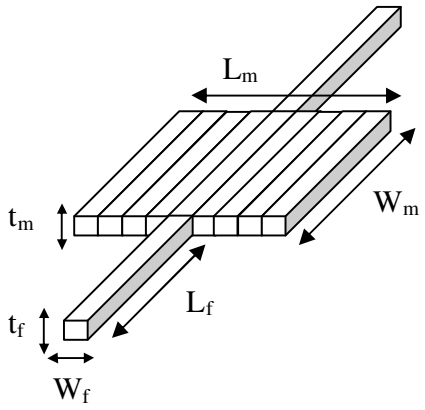


Figure 3-1 Illustrates the volumetric slits used for kinetic energy calculation of the scanning frame

The kinetic energy for a single slit can simply be calculated as:

$$dE_{kinetic} = \frac{1}{2}(\rho L_m t_m dx)\left[(x\dot{\sin}\theta)\right]^2 \tag{3-3}$$

where the dot above the brackets represents derivation with respect to time, (to find velocity from displacement) $W_m$ is the length of the mirror in the direction along the flexures, $t_m$ is mirror thickness, $\rho$ is the material density, $dx$ is the infinitesimal length and x is the position along the length, $L_m$, of the scanning frame. Neglecting the kinetic energy in the suspension springs, the total kinetic energy in the system can be calculated as:

$$E_k = \int_{\frac{-L_m}{2}}^{\frac{L_m}{2}} dE_k \tag{3-4}$$

For mechanical deflections as large as 20°, it can safely be assumed that $\sin(\theta) = \theta$. Then, the following integral gives the total kinetic energy in the system,

$$E_k = \int_{\frac{-L_m}{2}}^{\frac{L_m}{2}} \frac{1}{2}(\rho W_m t_m dx) x^2 \dot{\theta}^2 \tag{3-5}$$

After taking the integral,

$$E_k = \frac{1}{24} m L_m{}^2 \dot{\theta}^2 \tag{3-6}$$

where m is the mass of the scanning frame.

Now we can turn our attention to the computation of potential energy. The angular spring constant of a torsional scanner is given by

$$k_\theta = \frac{2K_{ab}}{L_f} \tag{3-7}$$

$K_{ab}$ is the shape factor incorporating *G* and given by [18]

$$K_{ab} = G\frac{W_f}{2}(\frac{t_f}{2})^3(\frac{16}{3} - 3.36\frac{t_f}{\mu W_f})\left[1 - \frac{1}{12}(\frac{t_f}{\mu W_f})^4\right] \tag{3-8}$$

where μ is the shape anisotropy constant that is equal to unity for isotropic materials. For FR4, μ can be taken as unity along the two common perpendicular *weft* and *warp* (or *fill* and *grain*) cut directions as the torsional modulus along those were measured to be about equal. Then, the potential energy stored in the flexures is calculated as follows:

$$E_p = \frac{1}{2} k_\theta (\theta)^2 \tag{3-9}$$

Using the Euler-Lagrange equation, the EOM can be written as below:

$$\frac{L_m{}^2 m}{12}\ddot{\theta} + k_\theta \theta = T_{mag} \tag{3-10}$$

In (3-10), the factor in front of $\ddot{\theta}$ term is the inertia, $J_m$, and the factor in front of $\theta$ is the spring constant. Then,

$$J_m = \frac{L_m{}^2 m}{12} \tag{3-11}$$

The resonant frequency of such a linear system is given by

$$f_{res} = \frac{1}{2\pi}\sqrt{\frac{k_\theta}{J_m}} \tag{3-12}$$

In (3-10), damping is not considered. To account for damping, the equation can be updated and finalized as below:

$$\frac{L_m{}^2 m}{12}\ddot{\theta} + b\dot{\theta} + k_\theta \theta = T_{mag} \tag{3-13}$$

where damping coefficient, $b$ is calculated from the experimentally measured quality-factor (Q) as

$$b = \frac{\sqrt{J_m k_\theta}}{Q} \tag{3-14}$$

## 3.2 FEM Analysis

Finite element analysis (FEA) techniques allow accurate modeling of mechanical structures. In this section, a sample scanner is modeled using FEA to validate the analytical calculations presented in section 3.1. The scanner, whose dimensions and material properties are summarized in Table 3-1. This scanner has copper laminates on both sides, which increases its effective torsional modulus and density, compared to values in Table 2-1. 3D modal analysis results of the scanner for the first five modes are shown in Figure 3-2. FEA predicts the torsion, which is the first mode, to be at 393Hz. Analytical calculations presented in section 3.1 predict torsion mode at 382Hz for the same material properties. The difference between the results is less than 3% and the two approaches look to be in agreement.

A full material model of FR4 requires orthotropic modeling, which requires 9 parameters, namely Young's modulus, shear modulus and Poison's ratio in all three dimensions. (x, y, z) However, since FR4 is being used for the first time as an actuated platform, all material properties are not known. Furthermore, the copper pattern on the FR4 structure significantly affects the composite properties. Hence, an FEA based modal analysis requires separate runs for each mode, where each run performs analysis assuming different linear material properties.

In order to extract the material properties relevant to the modes of interest, experimental measurements are conducted. The modal characterization of FR4 is done by LDV measurements. Then, material property values are iteratively found from FEM such that the FEA based and experimentally found frequency values match. This approach necessitates accurate modeling of inertia, since a wrong inertia modeling leads to wrong modal characterization in FEM, resulting in wrong prediction of material properties.

| Scanner Parameter | Symbol | Value |
|---|---|---|
| **Mirror width** | $W_m$ | 10mm |
| **Mirror length** | $L_m$ | 10mm |
| **Mirror thickness** | $t_m$ | 260µm |
| **Flexure thickness** | $t_f$ | 260µm |
| **Flexure length** | $L_f$ | 7mm |
| **Flexure width** | $W_f$ | 0.5mm |
| **Composite torsional modulus** | G | 7.8 GPa |
| **Composite Poison's ratio** | ν | 0.2 |
| **Composite density** | ρ | 3500 |

Table 3-1 Summarizes the sample torsional scanner dimensions and material properties.

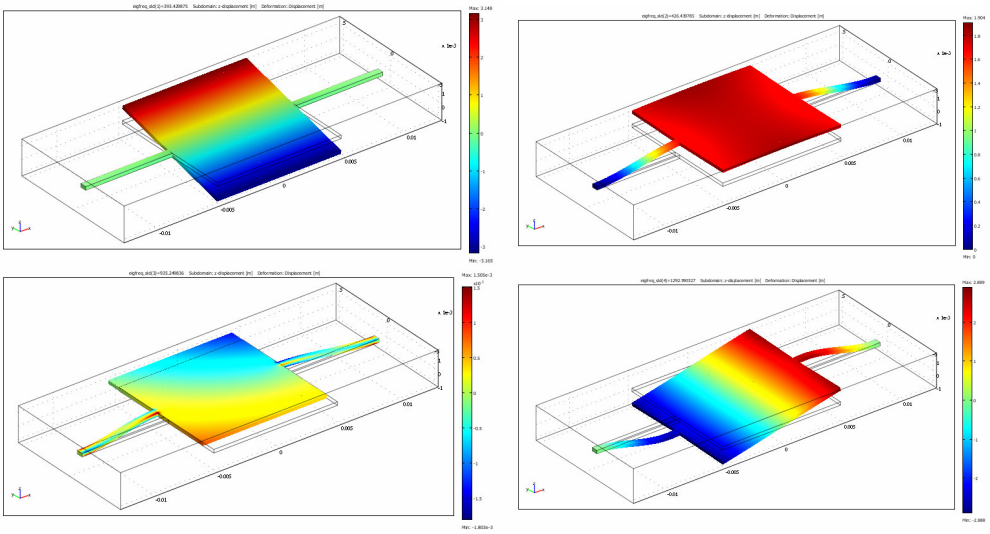

Figure 3-2 Shows the result of 3D modal analysis of a sample FR4 scanner. ($f_1$ = 393Hz, $f_2$ = 426Hz, $f_3$ =935Hz, $f_4$ = 1292Hz)

# 4 MAGNETIC ACTUATION SCHEMES

As briefly discussed in chapter 2, FR4 scanners can be actuated with various techniques. In this section, these electromagnetic actuation schemes are studied in detail. In section 4.1, soft magnetic film actuation is discussed for dynamic deflection case, together with experimental verification of the theoretical model. In 4.2, moving magnet actuation is investigated. Section 4.3 discusses moving coil actuation with FR4 scanners.

## 4.1 Soft-Magnetic Film Actuation

Soft magnetic films can be used for actuating structures with electromagnetic forces. These actuators can either be made of a thin ferromagnetic substrate or they can have a plated/coated/mounted magnetic film layer on a different structural layer.

Magnetic film actuators can be excited with external electro-coils. The magnetic field produced by the coil magnetizes the ferromagnetic layer on the actuator. Then, the magnetized sample tries to align itself with the external field, which creates the torque. More specifically, the component of magnetic field along the magnetic film plane magnetizes the film. The normal component of the field tries to rotate the sample so as to align the magnetization vector of the film with its own field. This torque is called the *magnetic anisotropy torque*.

FR4 platform allows making of such actuators very easy since the copper layer on FR4 can be used as a seed metallic layer for deposition. The torsional scanner with the

geometry summarized in Table 3-1 is plated with permalloy for soft magnetic film actuation. The actuator is illustrated in Figure 4-1.

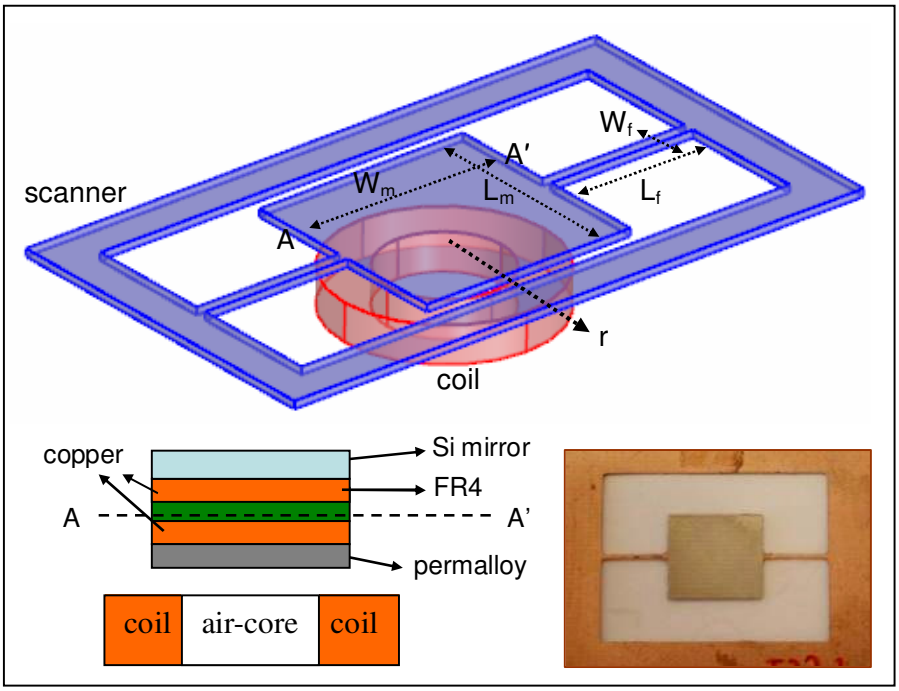


Figure 4-1 (Top) Illustration of the FR4 scanner and the actuation coil underneath; (Lower left) AA' cross section illustrating different layers and the coil; (Lower Right) picture of the NiFe plated scanner.

The scanner is fabricated using a 200 µm thick FR4 with double-sided copper laminates using standard printed circuit board (PCB) technology [10]. A permalloy sheet with average thickness of 15 µm is plated on the copper laminate and an external coil is used for actuation. In this system, the magnetic field on the permalloy layer is not uniform as the Ni-Fe plated region and the electro-coil have comparable footprint areas resulting in curved magnetic field lines across the permalloy film. Hence, even at large magnetic field values, certain regions on the magnetic film where the field lines are nearly perpendicular

to the film plane would not be saturated. Therefore, an accurate model is needed to account for the magnetic hysteresis effects for dynamic actuation.

In the following sub-sections, a new model to calculate the magnetic torque on a soft magnetic film in nonuniform fields is developed. Section 4.1.1 investigates electro-coil modeling with FEM analysis, which is required to calculate the magnetic field to be used in torque calculations. In 4.1.2, the magnetic torque calculation technique is studied in detail. Section 4.1.3 presents a new analytical function to model the magnetic hysteresis of ferromagnetic materials, which is essential for studying dynamic deflections. Sections 4.1.4 and 4.1.5 provide experimental results and model verification.

### *4.1.1 Electro-coil Modeling*

The actuation coil used in the system has a radius of 10mm and a height of 3.5mm. Therefore, the electro-coil and the permalloy film have comparable footprint areas, which results in highly nonuniform magnetic field across the magnetic material. Finite element modeling (FEM) of the electro-coil with *Comsol Multiphysics 3.3*® is performed to calculate the nonuniform magnetic field across the magnetic film. A circular air-core electro-coil is used for accurate and fast axially symmetrical simulations. The vertical and radial magnetic field obtained from FEM is exported to a numerical routine in MATLAB® to calculate the distributed moments. Figure 4-2a shows the experimental magnetic field measurements using teslameter and FEM simulation results of the perpendicular field ($B_z$) and Figure 4-2b shows the FEM result for the radial field ($B_x$) of the coil. The experimental data is obtained by first placing the teslameter at the center of the coil, and then moving it along the horizontal axis using a micrometer. Both vertical and horizontal magnetic field values substantially change with radial distances of a few millimeters, which clearly reveals the need for a model capable of handling non-uniform magnetic fields.

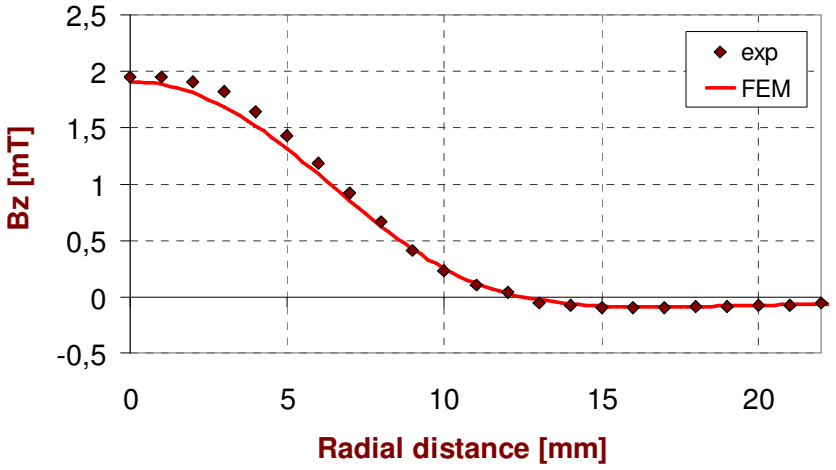


(a)

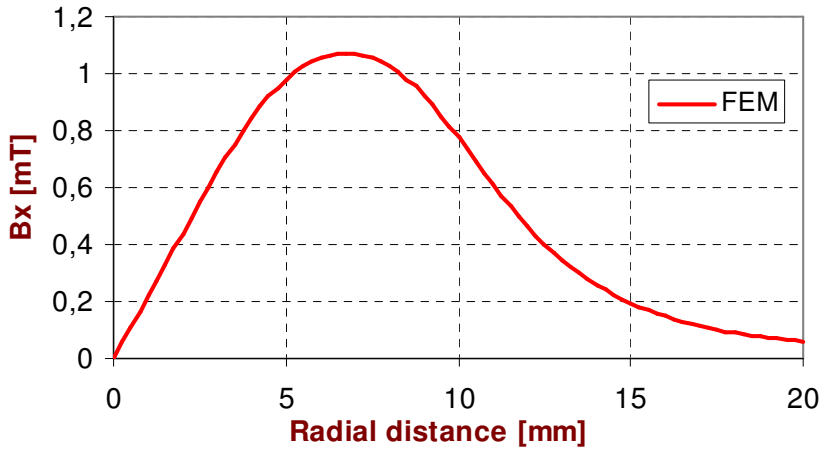


(b)

Figure 4-2 (a) The experimental and FEM simulation results of vertical magnetic flux density ($B_z$) for 35 mA rms coil current. Vertical flux density measurements are taken as a function of radial distance from the coil along the r vector shown in Fig.4.1, by moving the teslameter tip with a micrometer. (b) FEM simulation results for radial magnetic flux density ($B_x$) for the same current along r vector. The outer coil dimensions for radius and thickness of the air-core coil are 10mm x 3.5 mm, respectively

### *4.1.2 Magnetic Torque Modeling*

In an ideal hard magnetic material (permanent magnet) the magnetization vector does not change its magnitude and it does not rotate away from the preferred axis (easy axis). However, in soft magnetic materials the magnetization vector can rotate away from its initial preferred position. Nevertheless, the length and the width of the permalloy layer in the torsional FR4 scanner is 10 mm x 10 mm whereas the thickness of the film is 15 μm. So, the thickness to length and width ratio of the film is very small (<0.002); therefore, the shape anisotropy is dominant in setting the magnetization direction of the permalloy film. Other directionality factors such as crystalline or stress anisotropy [20] are ignored in the model. Due to the shape anisotropy, the magnetization vector remains in-plane and the out-of-plane component of the magnetization vector is neglected. The magnetic model for torque calculation is illustrated in Figure 4-3 across the cross-section AA′.

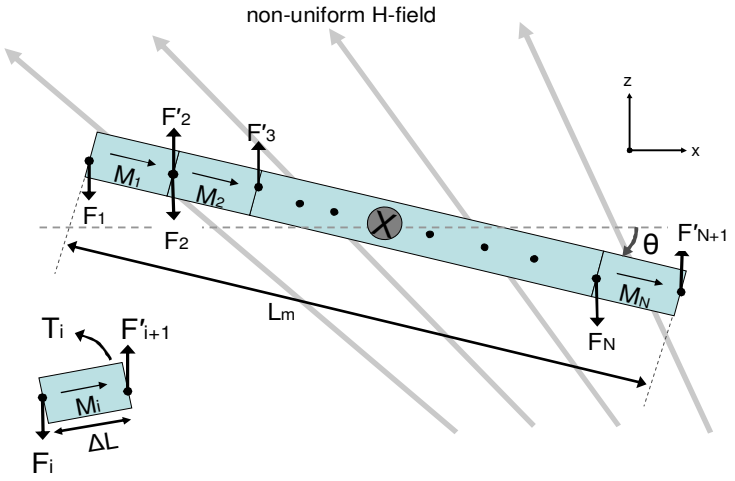


Figure 4-3 Moments ($T_1$,$T_2$...$T_N$) and forces ($F_1$, $F_2$, $F_2$',...,$F_N$,$F'_{N+1}$) acting on the magnetic material volume elements. Figure inset shows a single volume element

The magnetic film is divided into a grid of $N$ volumetric elements with uniform thickness ($t_p$), width ($W_m$) and length $(L_m/N)$ where each element has a respective magnetization direction determined by the magnetic field vector at that location. Due to the shape anisotropy, magnetization vector remains in-plane and each magnetized volumetric element can be treated as a permanent magnet with time-varying magnetization determined by the incident field and the material permeability. Therefore, thin magnetic films can be modeled as an array of permanent magnets. [21]

The distributed forces on each element, shown in Figure 4-3, are multiplied by the corresponding distances to the moment arm, i.e. torsion axis, to obtain the corresponding torque. Finally, contribution from every section is superposed to find the total net torque. The model is valid in non-uniform external fields for both saturated and unsaturated magnetic material cases, taking magnetic hysteresis effects into account.

The magnetic field incident on each element is different, i.e. the north and south poles of each magnetized sample experiences fields $H_i$ and $H_{i+1}$, respectively. In this case, force equations for a single element should be written as follows: [24]

$$\begin{aligned} F_1 &= M_1 \cdot W_m \cdot t_p \cdot H_1 \\ F_2^{'} &= M_1 \cdot W_m \cdot t_p \cdot H_2 \\ F_2 &= M_2 \cdot W_m \cdot t_p \cdot H_2 \\ F_N &= M_N \cdot W_m \cdot t_p \cdot H_N \\ F_{N+1}^{'} &= M_N \cdot W_m \cdot t_p \cdot H_{N+1} \end{aligned} \tag{4-1}$$

where $H_i$ is the z-component of the magnetic field incident on $i^{th}$ volume element (z-direction is taken as shown in Figure 4-3). If the magnetic film is single domain, all elements would have the same magnetization and the net force would simplify to

$F_{NET} = F_1 - F_{N+1}^{'}$, which is consistent with [24] when N= 1. The net force on the mirror tries to actuate the device in the pumping mode. However, torsional resonator with Q~100 is a very good mechanical filter at the torsional resonance frequency and its response to out-of-plane forces is very small. Thus the effect of net force can be neglected. The moment generated by these forces results in torsional actuation; hence it is assumed that all the deflection is due to the net moment (or torque) on the scanner.

The moment due to each volumetric element is simply calculated by multiplying the force by the distance to the torsional axis.

$$T_N = (F_{N+1}^{'} - F_N)\Delta L\cos(\theta) \tag{4-2}$$

where ΔL is the length of each volumetric element and θ is the angular deflection. Therefore the net torque is

$$T_{NET} = \sum_{i=2}^{N} T_i \,, \tag{4-3}$$

If the external magnetic field is uniform, all forces and moments cancel except for the two at each end and the net torque becomes

$$T_{NET} = (W_m t_p L)MH = VMH\cos(\theta) \tag{4-4}$$

where $V$ is the volume of the magnetic material. This expression of torque is consistent with [25].

In a general form, the driving current is a sinusoid at a frequency of w/(2π) with a DC offset. In addition to the current offset, an external permanent magnet can also contribute to

the DC components of the magnetic field and magnetization. Therefore, (4-4) can be written as below, assuming that the magnetic field oscillation is at frequencies where magnetization can follow the field oscillations:

$$T_{NET} = V(M_{DC} + M_{AC}\sin(wt))(H_{DC} + H_{AC}\sin(wt)) \tag{4-5}$$

If the offset current is zero and there is no DC field from a permanent magnet, the net torque simplifies to

$$T_{NET} = \frac{V}{2} M_{AC} H_{AC} (1 - \cos(2wt)) \tag{4-6}$$

assuming that the AC field is not saturating the magnetic film. In this case, the net torque given by (4-6) has a DC component and an AC component at twice the frequency of the drive current. Additionally, changing the direction of the current has no effect on the direction of the net torque, since the sign of $M_{AC}H_{AC}$ product is always positive, resulting in a unidirectional torque. If the AC field is much larger than the saturation magnetic field, $M_{AC}$ can approximately be considered as switching back and forth between +/-$M_{sat}$ at the frequency of the driving current and then the net torque becomes

$$T_{NET} = \frac{V}{2} \left| M_{AC} H_{AC} \sin(wt) \right| \tag{4-7}$$

whose harmonic at 2ω is four times larger than that at ω. Therefore, if there is no offset in the excitation current, net torque is always unidirectional and largest deflections are obtained when the driving frequency is at half of the mechanical resonance frequency.

When the excitation current has a large DC and a small AC component, variations in the magnetization can be neglected. The same approximation can be made if a strong DC

field is incident on the magnetic film due to a permanent magnet. In this case, the net torque can be written as

$$T_{NET} = V(M_{DC})(H_{DC} + H_{AC}\sin(wt)) \tag{4-8}$$

Then, the net torque becomes bidirectional and the frequency of the forcing function is the same as the driving current frequency. Hence, in this case, current should be applied at the exact mechanical resonant frequency for achieving maximum scan angle.

Plugging in the torque calculated by the model presented in this section into (3-13) and solving the differential equation of motion, the angular deflection of the torsional scanner as a function of time can be obtained.

### *4.1.3 M-H and B-H Loop Modeling*

Magnetization of ferromagnetic materials is a process of memory. In other words, the value of magnetization of such a material is not only a function of the external magnetizing field, but it also depends on the previous magnetization state. This is due to the fact that ferromagnets are made up of *magnetic domains*. Each domain has magnetic dipoles aligned in the same direction and one domain is separated from another with the so called *domain wall*. In the magnetization process, these domain walls move to make those domains aligned with the external field larger whereas the domains not aligned with the magnetizing field shrink. Therefore, once all dipoles are aligned with the external field, material becomes single domain and the total magnetization of the ferromagnetic material cannot get larger although the external field is increased. This is called the *magnetic saturation*. Therefore, magnetization of a ferromagnetic material is a nonlinear process. Furthermore, the domain wall movement is irreversible to some extent, which means some domains prefer to keep their orientations even though the external field is switched off. Therefore, in

order to make all domains randomly polarized, magnetic field with reversed direction should be applied rather than simply turning off the external field. This causes a *hysteresis*, i.e. memory, in the magnetization process. Therefore, a typical magnetic hysteresis loop (also called *B-H loop*) looks similar to the loop shown in Figure 4-4.

For dynamic actuation of the soft magnetic film actuated scanners, the magnetic field is alternating. Therefore, the time varying magnitude change of the field causes a time varying magnetization strength in the ferromagnetic material. In this case, the M-H loop of the magnetic film is being traced at each cycle of oscillation. This necessitates taking magnetic hysteresis into account for accurate magnetic torque modeling, especially for cases when the magnetic material is not saturated.

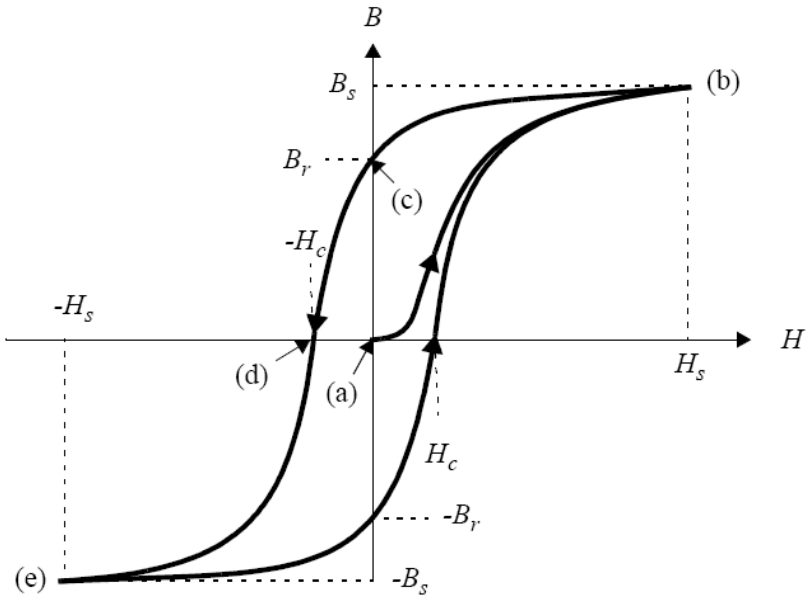


Figure 4-4 A typical B-H loop for a ferromagnetic material

M-H loop of the magnetic film is modeled using a new and simple function, whose parameters make it ideal to be used as a fit function to the actual M-H loop of the ferromagnetic materials. The function proposed in this paper to model magnetic hysteresis is as follows:

$$M(H_r) = M_{sat} - 2M_{sat} / \left(1 + \exp(\frac{H_r - H_c}{D})\right) \tag{4-9}$$

where $M_{sat}$ is the saturation magnetization, $H_r$ is the radial component of the external magnetic field on the magnetic element, which is responsible for magnetizing the sample, $H_c$ is the coercivity of the ferromagnetic material, and $D$ is related to the relative permeability of the material. As $D$ is increased, permeability decreases. The fact that this function has independently controllable parameters for each critical value of a hysteresis loop and that it converges to +/- $M_{sat}$ for large values of positive and negative magnetic fields make it a rather easy and suitable fit function for M-H loop modeling.

The D parameter in (4-9) can be related to the relative permeability using basic electromagnetic relations. M and H are related through susceptibility, $\chi$ as follows: [26]

$$M(H_r) = \chi(H_r) H_r \tag{4-10}$$

The equation for relative permeability as a function of $\chi$ is given by

$$\mu_r(H_r) = (\frac{\chi(H_r)}{\mu_0} + 1) \cong \frac{\chi(H_r)}{\mu_0} \tag{4-11}$$

The approximation above is valid when $\chi/\mu_0$ is much larger than unity, which is the case for ferromagnetic materials. Then, the relative permeability can be calculated by differentiating M with respect to $H_r$ and by using (4-11) as follows:

$$\mu_r(H_r) = \frac{1}{\mu_0}\frac{\partial M(H_r)}{\partial H_r} \tag{4-12}$$

The peak permeability, $\mu_{max}$ can be found by evaluating (4-12) at $H_r = H_c$, which reveals the relation between the $D$ parameter in (4-9) and $\mu_{max}$:

$$D = \frac{M_{sat}}{2\mu_{\max}\mu_0} \tag{4-13}$$

Therefore, all the parameters of (4-9) have physical meanings, which make the new M-H loop function proposed here very useful. In order to relate the M-H loop to the B-H loop, the relation below can be used which simply requires adding a linear term to the M-H loop function. [26]

$$B(H_r) = \mu_0 H_r + M(H_r) \tag{4-14}$$

The remanent flux density, $B_r$ which is the magnetic flux density remaining in a previously magnetized ferromagnetic material in the absence of external magnetic field, can simply be obtained by evaluating (4-9) at zero magnetic field, which yields

$$B_r = M_{sat} - 2M_{sat} / \left(1 + \exp(\frac{H_c}{D})\right) \tag{4-15}$$

where $B_r$ denotes the remanent flux density. In order to account for the hysteresis effect, the same function is used with $H_c > 0$ for forward sweep and $H_c < 0$ for backward

sweep of magnetic field, which simply results in a shift along +/- x direction of the same function. For the initial magnetization of the sample, $H_c$ should be taken as zero. Figure 4-5 shows the M-H loop function based on (4-9) and the relative permeability for forward sweep with arbitrary values of the parameters for demonstration purposes.

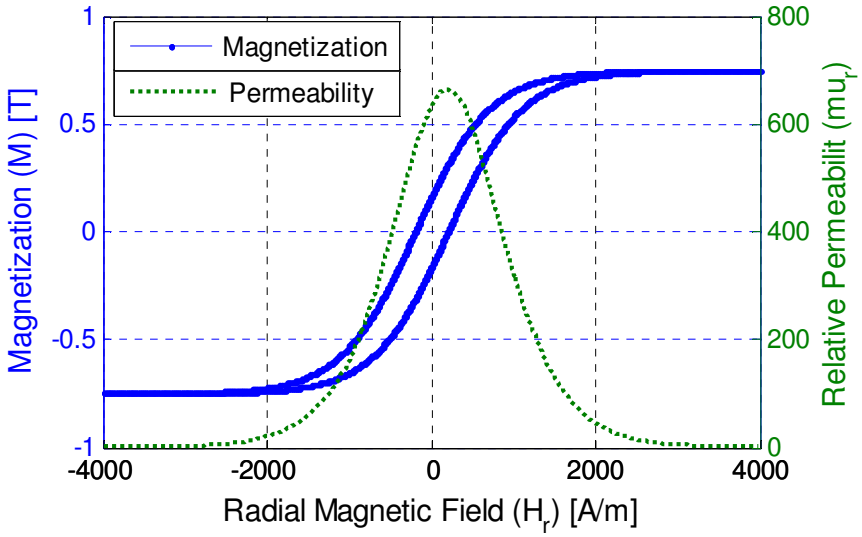


Figure 4-5 Exemplary M-H loop using (5) for Msat = 0.75T, Hc = 200A/m, D=450 and corresponding relative permeability for the forward sweep of $H_r$.

### *4.1.4 Magnetic Model Verification*

Maximum velocity at the tip of the sinusoidally vibrating scanner is measured with a *laser doppler vibrometer* (LDV) while avoiding specular reflections back to the LDV. Rotation angle can be calculated using the mirror size and the operation frequency.

Figure 4-6 shows experimental results and calculations for the torsional scanners using the model developed in the previous section. For this experiment, the scanner is

moved along the *r*-direction shown in Figure 4-1. Experimental data is used to obtain the effective magnetic parameters for the permalloy film. Best fit to the experimental data is obtained using the M-H loop function given in (4-9) with $\mu_r$=600 and $M_{sat}$=0.85T. Since the applied magnetic field is large and M-H loop is narrow, $H_c$ is taken as 0, i.e. hysteresis is neglected.

The deflection is a function of both $M$ and $H_z$. Since $M$ is related to the radial magnetic field with the M-H loop of the magnetic material, $H_rH_z$ product of the magnetic field due to electro-coil determines the deflection of the scanner. Therefore, as illustrated by Figure 4-6, the deflection is maximized at about 6mm radial distance from the coil top where the sum of distributed $H_rH_z$ product attains its maximum value. Deflections are lower in regions close to the center of the coil where $H_r$ is small and in regions far from the coil where $H_z$ is small. The theoretical calculations based on the model and the experimental measurements are in good agreement.

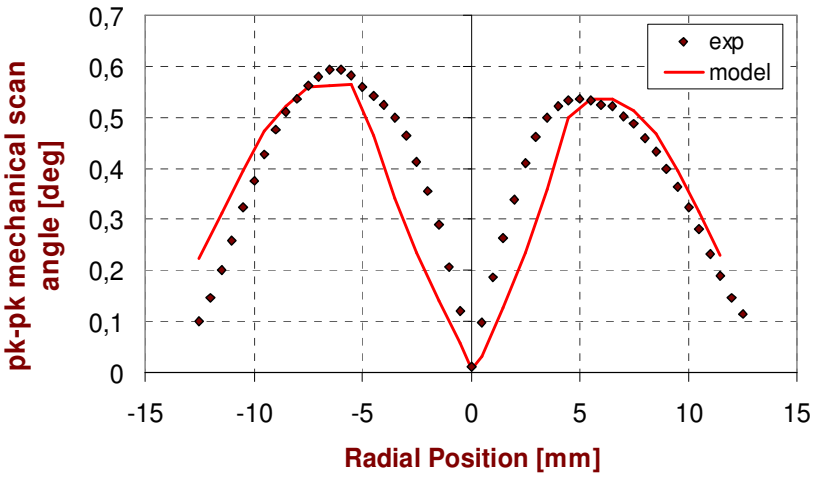


Figure 4-6 The experimental and theoretical results of AC tip deflection vs. scanner position over the coil at 40 mA rms current. Scanner is operated at low scan angles.

Figure 4-7 shows the theoretical and the experimental tip deflections at $r$=-6mm as a function of the rms coil current. The same magnetic material properties are used for the theoretical calculations. It is important to note that deflection increases quadratically with increasing current up to about 25mA (rms). From this point on, the curve follows a linear trend. Once the magnetic material becomes single domain at a certain current level, magnetization reaches a saturation value and deflection becomes proportional to $M_{sat}H_z$ product, resulting in the linear relationship between deflection and current. As shown in Figure 4-7, the model successfully accounts for that effect.

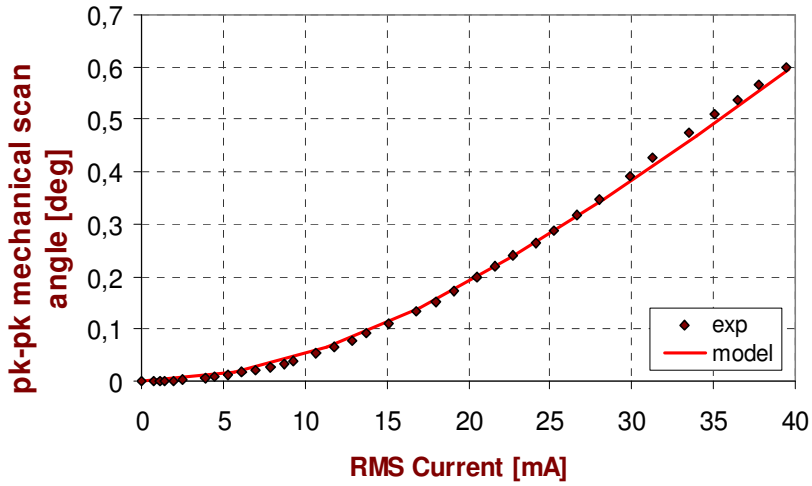


Figure 4-7 The experimental and theoretical results of AC tip deflection as a function of rms current at r=-6mm radial distance from the coil. The curve makes a smooth transition from quadratic to linear relationship between deflection and current between 15mA and 25mA rms coil current, where saturation occurs. Scanner is operated at low scan angles.

### *4.1.5 Hysteresis Demonstration with a Torque Magnetometer*

The experimental results presented in the preceeding section are obtained at relatively large magnetic fields compared to the coercivity of the magnetic film. Therefore, hysteresis

effects are not observed and the nonlinear permeability model without hysteresis effects (i.e., $H_c$=0) works well. However, for low deflection regimes where magnetic field is cycling at low amplitudes comparable to the coercivity values, the effect of hysteresis and magnetic memory become apparent. To demonstrate the accuracy of the model presented for low magnetic fields and small deflections, the torsional scanner was utilized as a torque magnetometer. An approach similar to [28] was followed to extract the M-H loop information accurately. In the same setup illustrated by Figure 4-1, a DC sweep of the coil current was performed from -60mA to 60mA, both in the forward and backward directions to trace the M-H loop of the permalloy film. A constant small AC current of 0.25mA was applied on top of the offset current to vibrate the actuator at resonance. In this case, force is bidirectional, as discussed in section 4.1.2, and resonant actuation is achieved by applying current at the mechanical resonance frequency of the scanner. Figure 4-8 shows the results of this experiment and the theoretical prediction of the model. Peak-to-peak deflection tends to become constant despite the increasing offset current on the coil, since magnetic film reaches saturation at large coil currents. The lowest deflections in forward sweep and backward sweep of offset current are obtained at different nonzero current values of the external field due to the memory of the permalloy film. This observation is a clear evidence of the magnetic hysteresis effects. AC deflections during backward current sweep are shown as negative for illustration purposes. As clearly seen, the magnetic model presented in this work can accurately predict the deflection of the actuator both for saturated cases and unsaturated cases under very low magnetic fields.

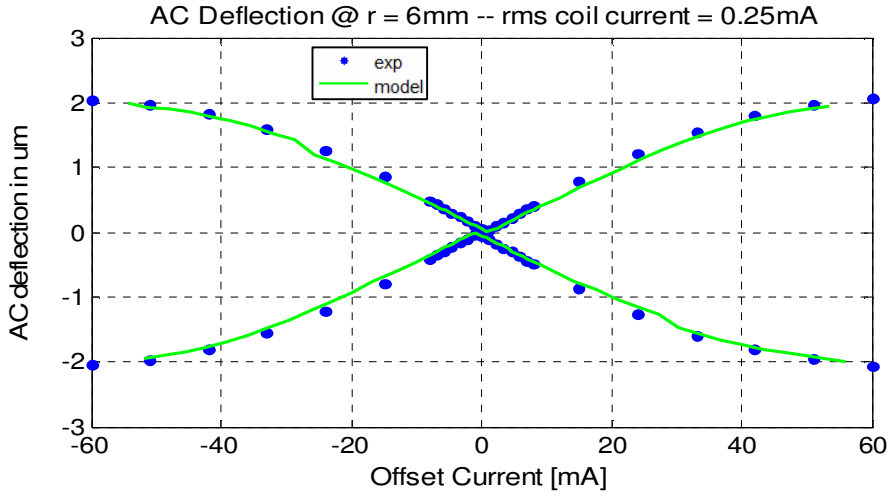


(a)

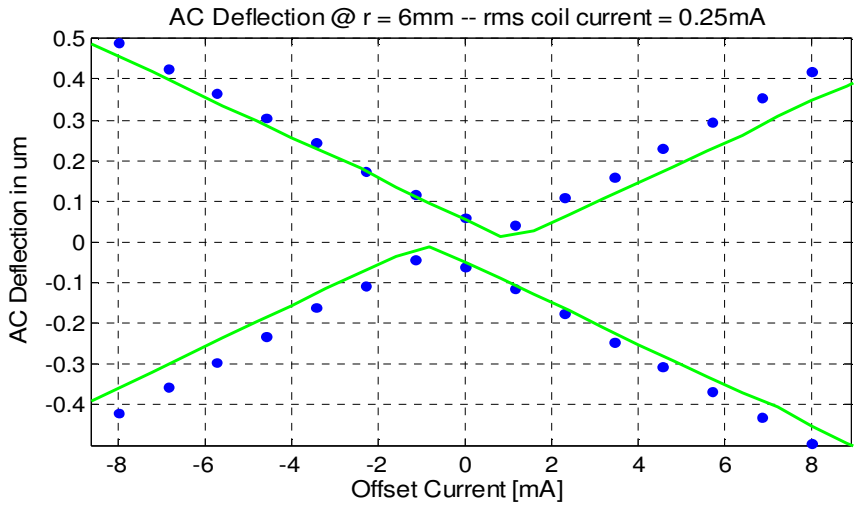


(b)

Figure 4-8 (a) The experimental and theoretical results of peak-to-peak deflection as a function of DC offset current. A forward offset sweep (shown as positive deflection) and backward offset sweep (shown as negative deflection) reveals the hysteretic behavior of the magnetization of the sample. (b) The same plot with different scale to better illustrate coercivity and remanence values.

Figure 4-9 shows the magnetic hysteresis function that was used to fit the above experiments. A narrow hysteresis loop is observed, which is expected of permalloy films. According to the model, the saturation flux density of the permalloy film is 0.85T, its maximum relative permeability is 615, corresponding to D = 550, coercivity is 27 A/m and remanent flux density is 20mT.

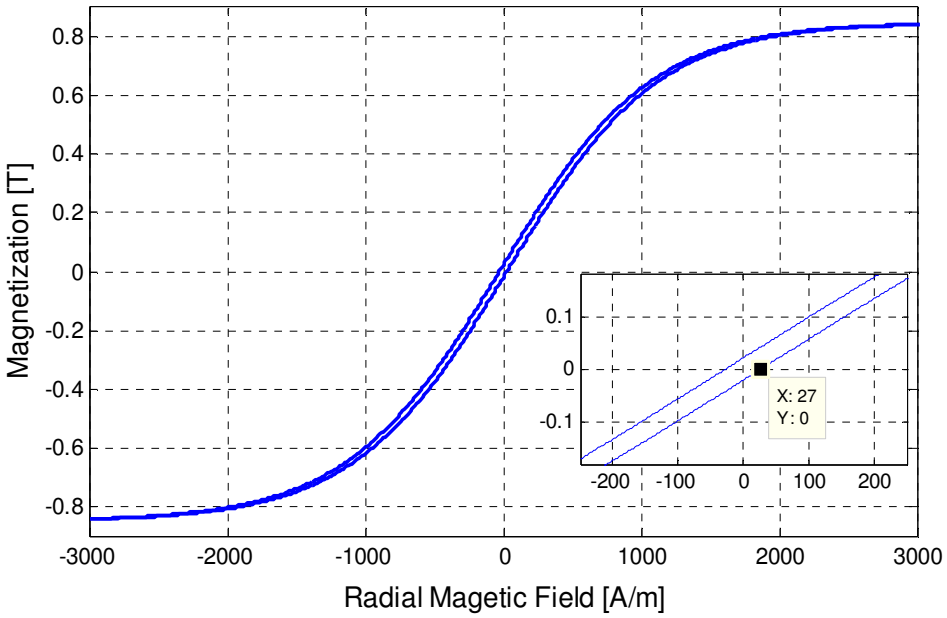


Figure 4-9 Calculated M-H loop of the permalloy film using the proposed hysteresis function. Saturation flux density is found to be 0.85T, maximum relative permeability is 615 and coercivity is 27 A/m. Figure inset shows a zoom-in of the region around origin.

### *4.1.6 Scaling of the Magnetic Model for MEMS Devices*

The devices used to present and validate the dynamic magnetic actuator model in this paper are millimeter sized torsional scanners. However, the model developed here is applicable to microsystems and devices as well. Table 4-1 summarizes the effects of

scaling on device operation, with *s* being the scaling parameter. The change of quality factor with scaling is not taken into account in this chart. Therefore, the arguments in this section are valid for off-resonant excitation. So long as the coil current is kept constant, scaling all the geometrical dimensions of the system does not affect the scanning performance of the system because the stiffness of the device scales by the same amount as the total torque generated. Although the scan angle remains the same, resolution of the scanner increases by s, which is desired for display and imaging applications. However, power consumption of the system scales by $s^3$, revealing an inherent advantage of MEMS based actuators, which is in agreement with [29]. In this scaling analysis, the effect of permalloy layer thickness on its relative permeability is ignored.

| **Input Parameters** | **Scaling** |
|---|---|
| All dimensions of the actuator | s |
| All dimensions of the coil | s |
| Coil-scanner gap | s |
| **Resultant Output Parameters** | **Scaling** |
| Mass moment of inertia | $s^5$ |
| Angular Stiffness | $s^3$ |
| Resonance frequency of the scanner | 1/s |
| Magnetic field | 1 |
| Magnetization | 1 |
| Permalloy volume | $s^3$ |
| Net magnetic torque | $s^3$ |
| Angular displacement | 1 |
| Scanner resolution (proportional to mirror size x scan angle) [30] | s |
| Scanned pixels per second (resolution x frequency) | 1 |

Table 4-1 The effects of scaling on device operation, with *s* being the scaling parameter

## 4.2 Moving Magnet Actuators

In this section, torque calculation for moving magnet actuators is presented both for out-of-plane moving actuators and torsional scanners. A short discussion on the advantages and disadvantages of moving magnet actuators is provided.

### *4.2.1 Force Calculation for Out-of-plane Moving Magnet Actuators*

When a permanent magnet is placed in external magnetic field, it tries to minimize its magnetic energy. For the case where the magnetization of the magnet is aligned with the external field direction, there will be no net torque to rotate the magnet since the field is already aligned with magnetization. However, the energy in such a system is minimized when the magnet settles in the location where the magnetic field gradient is the maximum. Therefore, if the magnet is placed in field gradient, it tries to move without rotation as shown in Figure 4-10. In this case, the total force on the magnet can be calculated by

$$F_{net} = VM(H_{z1} - H_{z2}) = VM(\Delta H) \tag{4-16}$$

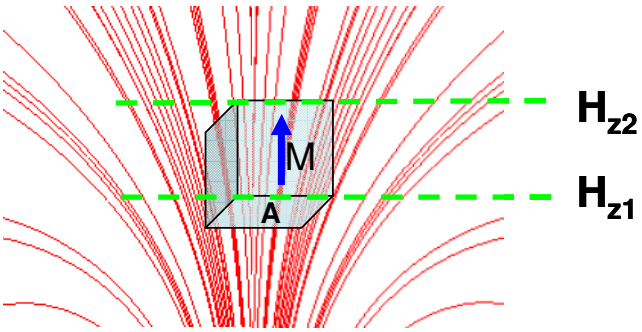


Figure 4-10 A moving magnet with its magnetization aligned with the external field inside a magnetic field gradient. Magnet tries to move downwards, toward the maximum field gradient.

Using this principle, out-of-plane actuators can be designed and produced using FR4. Figure 4-11 illustrates an out-of-plane actuated beam with a moving magnet. In this system, the cantilever beam can be dynamically actuated by alternating the magnetic field using an electro-coil.

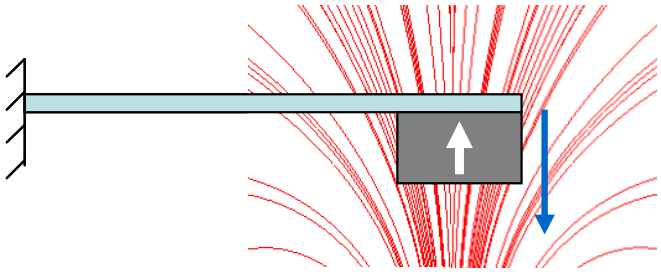

Figure 4-11 An out-of-plane actuated cantilever beam with moving magnet

### *4.2.2 Torque Calculation for Torsional Moving Magnet Scanners*

Moving magnet actuation for torsional scanners fundamentally relies on the same principle as the magnetic film actuated scanners. Actually, moving magnet actuation is a special case of magnetic anisotropy torque actuation, where the direction and magnitude of magnetization is always constant. Therefore, when a permanent magnet is placed in an external magnetic field with its magnetization vector aligned to make an angle θ with the field direction, it tries to align itself with the field to minimize its magnetic energy, creating a torque. In this case, the force on each pole of the magnet, as shown in Figure 4-12 can be written as follows, similar to (4-1):

$$\begin{aligned} F_1 &= M \cdot W_m \cdot t_p \cdot H_1 \cos(\theta) \\ F_2 &= M \cdot W_m \cdot t_p \cdot H_2 \cos(\theta) \end{aligned} \tag{4-16}$$

where $H_i$ is the component of magnetic field that is normal to the magnet plane. If the external field is uniform, then $H_1 = H_2 = H$ and the forces cancel each other, leaving a net torque that tries to rotate the magnet. Then, the net torque is calculated by multiplying the forces on each end by their distance to moment arm, which is the torsion axis.

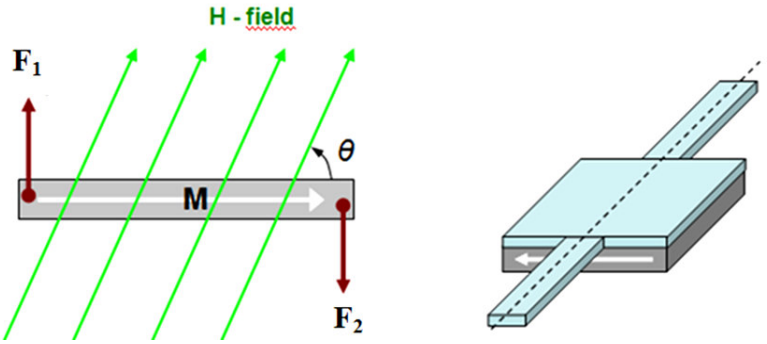


Figure 4-12 The forces on the poles of a permanent magnet placed in an external magnetic field

Then, the net moment is given by

$$T = M \cdot W_m \cdot t_p \cdot H \cdot \frac{L_m \cos(\theta)}{2} + M \cdot W_m \cdot t_p \cdot H \cdot \frac{L_m \cos(\theta)}{2} \tag{4-17}$$

Then, since $V = W_m\, t_p\, L_m$ where V is the volume of the magnet, net torque under uniform magnetic field simplifies to:

$$T = VMH\cos(\theta) \tag{4-18}$$

As suggested by (4-18), torque is bidirectional since the magnetization is pinned for a permanent magnet. Therefore, the maximum peak-to-peak deflection is obtained when the coil current is applied at the mechanical resonant frequency of the scanner, unlike magnetic

film actuation with zero DC bias current where the maximum deflections are observed when applied current is at half of the mechanical resonance frequency.

### *4.2.3 Discussion on Moving Magnet Actuation*

The main advantage of the moving magnet actuation is the large torque generation with low power-consumption compared to the soft magnetic film actuators. Since the volume of a magnet can be much larger than the electroplated films, much stronger forces can be generated. However, the cost of this approach is the reduced resonant frequency of the device due to the large inertia added by the magnet as suggested by (3-12). Additionally, the increased inertia causes the quality factor to drop. Depending on the application specific requirements, this may have some undesired implications. The magnet causes the center of mass of the actuator to move away from the rotational axis, which causes undesired vibrations of other modes of the structures. Another undesired implication of the added mass is the reduced shock tolerance of the structure due to the lowered natural frequency. Therefore, the optimization of the moving magnet actuators is critical to avoid such undesired effects.

### *4.2.4 Position Sensing with Moving Magnet Actuators*

One advantage of moving magnet actuators is that they allow position sensing by using a back-emf pick-up coil placed close to the moving magnet. The oscillating magnet modulates the magnetic flux density on a static coil wound close to the magnet. The changing flux density over the coil area creates a voltage acting against the source inducing it, known as the back-emf voltage. This effect is predicted by Faraday's law of induction as provided below:

$$\varepsilon = -N\frac{\partial \phi}{\partial t} \tag{4-19}$$

where N is the number of identical coil loops in the pick-up coil and $\phi$ is the total flux in the loop area.

FR4 offers a unique possibility for back-emf sensing in scanner systems. The copper on the static frame of the scanner can be patterned as a coil, which will pick up the electromagnetically induced voltage due to the moving magnet. Figure 5-2 shows a moving magnet scanner, where this idea is utilized. As shown on the figure, the back-emf coil is routed on the static frame. Although this is not an optimum coil for this application, a clear emf voltage is picked up as shown by Figure 4-13, when the scanner is oscillating at 30° peak-peak mechanical scan angle.

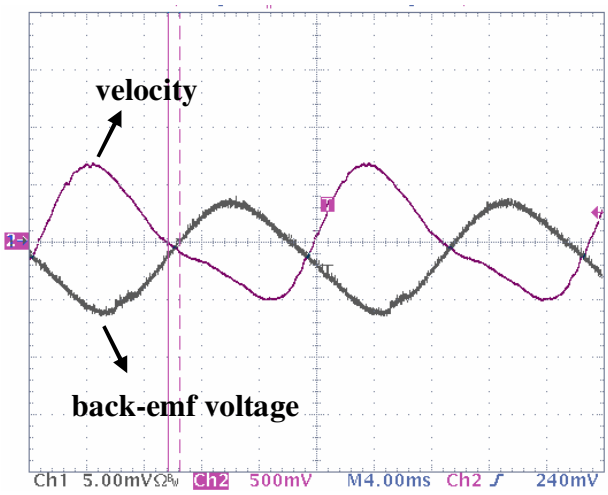


Figure 4-13 Velocity of the scanner and the back-emf signal produced on the pick-up coil

A novel FR4 scanner for large-angle scanning applications like display and imaging is designed and produced. Chapter 5 presents a detailed discussion of the design, development and characterization of a moving magnet scanner.

## 4.3 Moving Coil Actuators: Lorentz Force

### *4.3.1 Torque Calculation for Moving Coil Actuators*

As the name implies, moving coil actuators employ coils on their moving platform while the magnetic field is generated by an external static element. As shown in section 2.1, FR4 scanners can be actuated in the moving coil scheme by etching the copper layer on FR4 as a coil using PCB technology and using an external permanent magnet.

A moving charge experiences a magnetic force when an external magnetic field is incident on it. This force is called the *Lorentz force* and if there is no external electric field present, force is calculated as

$$F = Q(\vec{v} \times \vec{B}) \tag{4-20}$$

where Q is the total charge, ν is the velocity of charge and B is the magnetic field. Then, for line currents, the force on the wire can be calculated as

$$F = \int (\vec{v} \times \vec{B}) dq = \int (\vec{v} \times \vec{B}) \lambda dl \tag{4-21}$$

where λ is the line current density. Since the current through the wire is given by

$$I = \lambda v \tag{4-22}$$

The total force on a current carrying wire is given by

$$F = \int (\vec{I} \times \vec{B}) dl \tag{4-23}$$

Since $\vec{I}$ and $\vec{dl}$ always point in the same direction for a wire,

$$F = I\int(dl \times \vec{B}) \tag{4-24}$$

If the magnetic field is uniform over the conductor, force simplifies further to

$$F = I(\vec{L} \times \vec{B}) \tag{4-25}$$

For moving coil FR4 scanners, the current carrying conductor is a planar rectangular coil as shown in Figure 4-14 (also see Figure 2-1).

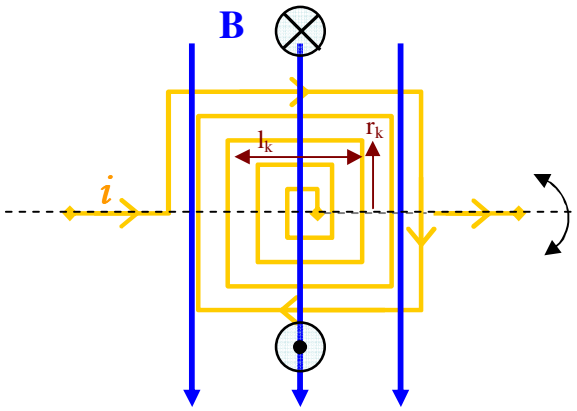


Figure 4-14 Shows the planar moving coil on FR4 scanners and the Lorentz force actuation

For torsional actuation, magnetic field is produced such that it does not change direction over the coil as shown in Figure 4-14. Then, the forces on either side of the torsional axis cancel each other, leaving a net torque with respect to the moment arm as shown in Figure 4-14. Assuming that the magnetic field is uniform across the coil, the net torque can be calculated by multiplying the force on each wire by its distance to torsion axis as shown below:

$$T = 2\sum_{k=1}^{N} B^{\perp} i l_k r_k \tag{4-26}$$

where $B^{\perp}$ denotes the perpendicular component of the magnetic flux density with respect to the current direction, N denotes the total number of turns in the coil, $l_k$ is length of one edge of the $k^{th}$ coil turn and $r_k$ is the distance of $k^{th}$ turn to the torsion axis. Then, assuming a square coil with edge length of $L_m$, at least 10 coil turns, and neglecting the gaps between the turns, the torque can approximately be calculated as:

$$T \cong \frac{iB^{\perp} N L_m^{\ 2}}{3} \tag{4-27}$$

Calculating the torque as given by (4-27) and plugging into the equation of motion given by (3-13), the angular deflection of the moving coil FR4 scanner can be calculated. It is worthwhile to note that the force generated in moving coil actuation is bidirectional. Therefore, to actuate the scanner at resonance with the maximum scan angle, the driving current frequency should be the same as the mechanical resonance frequency of the scanner.

### *4.3.2 Discussion on Moving Coil Actuation*

Moving coil FR4 scanners can be produced easily at low-costs since the copper layer on FR4 is patterned during the PCB routing process, eliminating the need for post-processing like permalloy plating and magnet bonding. In this sense, it is a convenient approach to take with FR4 scanners. Additionally, moving coil scanners have much less inertia compared to moving magnet actuators. Therefore, the flexures can be designed to be more compliant. Due to the low mass structures, shock resistance of moving coil scanners

is also better. However, the routing process brings some disadvantages with it. The spacing between two adjacent coil turns has to be as wide as the width of a single wire due to PCB design rules. Therefore, even using the best technology, the efficiency of using the planar FR4 area to pattern the coil is 50%, which means half of the moving platform area is actually not utilized for magnetic actuation. However, for moving magnet actuators, magnet covers the whole moving platform. Additionally, the external coils used for moving magnet actuation can be wound with almost 80% efficiency. Therefore, application specific requirements should be well identified to choose between moving magnet and moving coil design to achieve the largest scan angle with lowest power consumption.

A novel application of moving coil actuators for opto-mechanical systems along with experimental results is presented in detail in chapter 5. A more detailed comparison of moving magnet and moving coil scanners is provided in Appendix B.

# 5 TORSIONAL FR4 SCANNER WITH DYNAMIC FOCUSING

In this chapter, a novel torsional FR4 scanner is presented. The torsional scanner, which is designed for large-angle scanning applications, is integrated with a dynamic focusing module. This novel feature substantially increases the working range of the device.

Section 5.1 covers the basics of Gaussian optics to reveal the need for dynamic focusing in scanning systems. Section 5.2 describes the basic structure of the photonic module presented. Sections 5.3 and 5.4 give details of the scanning and dynamic focusing operations, together with experimental results.

## 5.1 Gaussian Beams and the Need for Dynamic Focusing

The light focusing module of a scan engine allows it to steer a focused spot on the surface of interest. If the focusing component is a passive lens with no dynamic focusing capability, the working depth of the scanner is limited due to divergence of the beam. When a Gaussian beam is focused with a lens, the spot size is smallest at the location called the *beam waist*. The spot size a Gaussian beam as a function of propagation distance is given by [31]

$$w(z) = w_0 \sqrt{1 + (\frac{z}{z_R})^2} \tag{5-1}$$

where $\omega_o$ is the spot size at the beam waist and $z_0$ is the *Rayleigh range* of the beam given by

$$z_R = \frac{\pi w_0^2}{\lambda} \tag{5-2}$$

where λ is the wavelength of the laser. Rayleigh range is the distance beam travels until its spot size gets $\sqrt{2}$ times larger than the focused spot size. In (5-1), z=0 is chosen as the coordinate of the beam waist, so that moving away from the waist location either towards +z or –z results in increased spot size as shown in Figure 5-1.

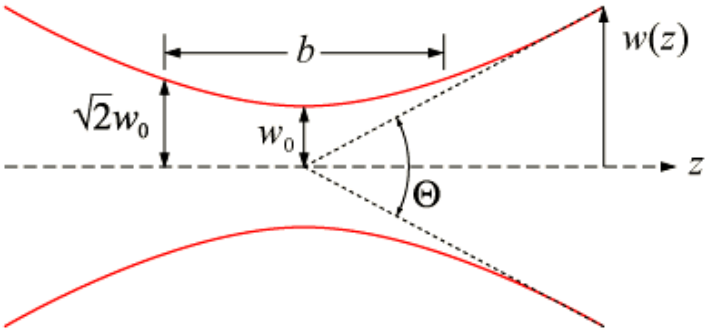


Figure 5-1 Shows the Gaussian beam profile along the propagation direction (figure taken from www.wikipedia.org)

The rate of increase of the spot size with the propagation distance is determined by the *divergence* of the beam. Divergence of a Gaussian beam is given by

$$\Theta = 2\frac{\lambda}{\pi w_0} \tag{5-3}$$

For a tight focused beam, $\omega_0$ is smaller and therefore divergence is higher. Hence, a tight focused beam gets out of focus faster. The *depth of focus* of a beam, which is the range where the spot size stays within $\sqrt{2}$ of its focused value, is given by

$$b = 2z_R = \frac{2\pi w_0^2}{\lambda} \tag{5-4}$$

The above discussion on the Gaussian optics reveals the fact that the depth of focus for a focused beam is shorter when the beam is focused to a smaller spot. However, small spot size is desired for scanning systems since this increases the *resolution* of the system. [30] Therefore, there is a trade-off in scan engine design between resolution and depth of focus, which defines the working range of the system. It is evident from this discussion that extending the depth of focus of scanning systems without compromising the resolution performance is of utmost importance.

Different solutions have been proposed in literature to extend the depth of field of scanning systems. Flexible optics such as liquid lenses [32] and deformable mirrors [33] have been used to achieve focal length modulation of the collimation optics. Refractive index modulation for dynamic focusing has been realized with acousto-optic [34] and liquid crystal lenses [35]. Scanners with moving lenses have also been devised [36].

In this research, variable focus laser light source integrated with an FR4 scanner using standard printed circuit board (PCB) technology is presented for the first time, which is an ideal platform for integrating electrical, mechanical and optical components as discussed in chapter 2. [10]

## 5.2 Structure of the Scan Engine

The scanner presented here is shown in Figure 5-2. The scanner is produced from a 300μm thick FR4 sheet. The torsional scanning frame is suspended by two torsional flexures. The dynamic focusing element (plunger with a laser diode at the tip) is cut inside

the scanning frame. The folded flexures holding the paddle, which carries the vertical cavity surface emitting laser diode (VCSEL), are designed to make the laser plunger structure compliant to reduce the power requirement. The laser diode on the plunger is translated out-of-plane with respect to a fixed focusing lens that is placed on the scanning frame to achieve dynamic focusing.

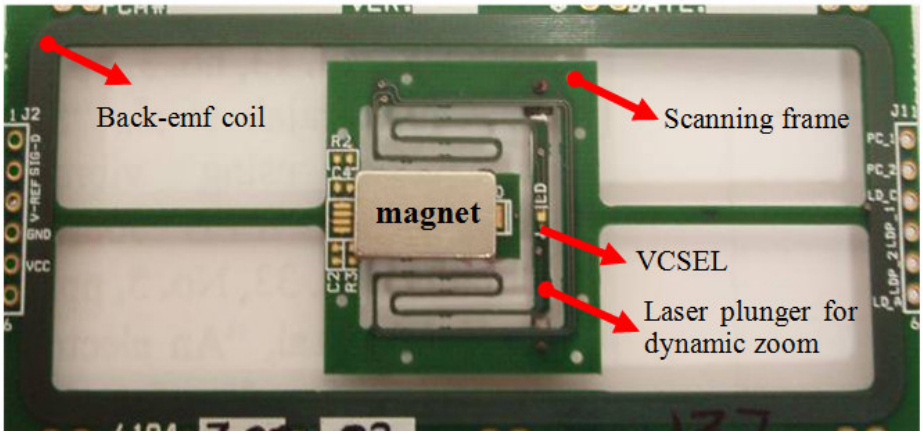


Figure 5-2 Picture of the torsional scanner integrated with a laser plunger element for dynamic focusing produced by conventional PCB technology. The torsional frame is suspended by two flexures and the laser plunger element is carved inside the torsional platform.

## 5.3 Torsional Scan Operation

Torsional scanning is achieved by physically scanning the VCSEL placed on the plunger rather than bouncing the beam from a scanning mirror. This approach makes the dynamic focusing practical and results in a highly integrated photonic module. The torsional actuator is of moving magnet type. A neodymium permanent magnet of dimensions 12x7x2 mm is mounted on the scanning frame. The magnet is poled in-plane and normal to the flexures. A 3mm thick external coil with a radius of 10mm is used for

resonating the scanner at 60Hz. 50° peak-to-peak mechanical scan angle is achieved at 80mW rms power. Since the laser is scanned physically, mechanical scan angle is equal to the optical scan angle.

Figure 5-3 shows the peak-to-peak mechanical deflection angle of the scanning frame as a function of coil drive current. As seen from the figure, the efficiency of torsional drive reduces at large deflection angles due to the change in magnet-coil distance.

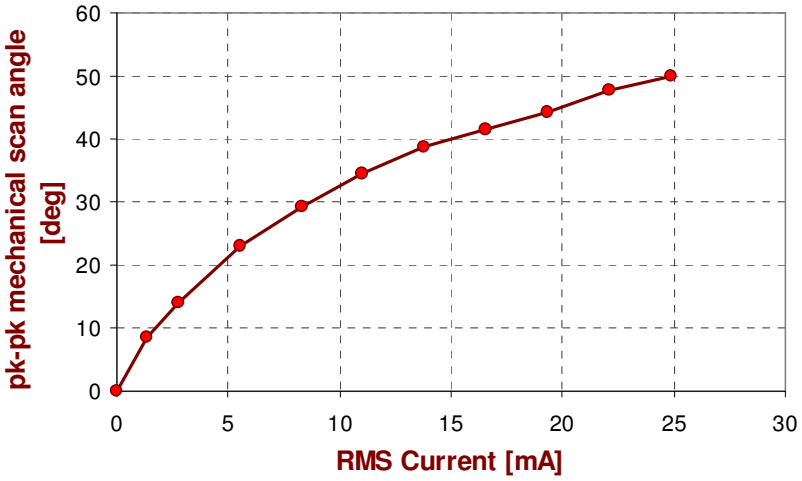


Figure 5-3 The peak-to-peak angular mechanical deflection of the torsional scanner as a function of power consumed in the torsional drive coil. The nonlinearity in the curve is due to magnetic tuning resulting from large deflections.

## 5.4 Dynamic Focusing Operation

### *5.4.1 Structure and Operation*

The main function of the integrated dynamic focusing feature on the torsional scanner is to allow pointing the laser beam to a point in the field of view of the scanner with a

focused spot. As discussed in section 5.1, dynamic zooming feature becomes valuable for applications requiring small spot size in a range longer than the Rayleigh range of the beam.

A moving coil actuated laser plunging element is cut inside the scanning platform to allow for out of plane deflections of the laser diode. A VCSEL is wire-bonded to the electrical connections on the paddle of the plunger, which is suspended by two folded arms to increase compliance. The plunger arms connect to the scanning frame. Four copper lines are routed on the 0.5mm wide plunger arm, one of which is for electrical connection to the laser and three for magnetic actuation of the moving coil plunger. An external permanent magnet is placed underneath the plunger paddle with sufficient clearance for deflections. The magnetic field of this magnet interacts with the current through the paddle to actuate the plunger out-of-plane with Lorentz forces. A 6mm focal length lens with 2.8mm diameter is mounted on the scanning frame with a plastic opto-mechanical holder. This optical unit moves with the torsional scanning frame. Figure 5-4 shows a picture of the moving coil laser plunger together with a drawing of the focusing optics assembly mounted on the torsional frame.

As the plunger is actuated, its paddle moves out-of-plane modulating the distance between the laser diode and the fixed focusing lens, varying the output beam waist distance from the scanner. The beam waist location can be calculated using the imaging equation, with its modified version for Gaussian beams derived by Self [37]

$$\frac{1}{d_0 + z_R^2/(s-f)} + \frac{1}{d_i} = \frac{1}{f} \tag{5-5}$$

where $d_o$ denotes the laser diode distance to the lens and $d_i$ denotes the beam waist (image) location and $f$ is the focal length of the lens.

Small deflections of the plunger tip results in a long shift of the focused spot depth due to large longitudinal magnification of the system. To avoid mechanical coupling of the torsion mode to the plunger operation, out-of-plane deflection mode of the plunger is designed to be at 150Hz and the actuation is off-resonant for controllability of the plunger.

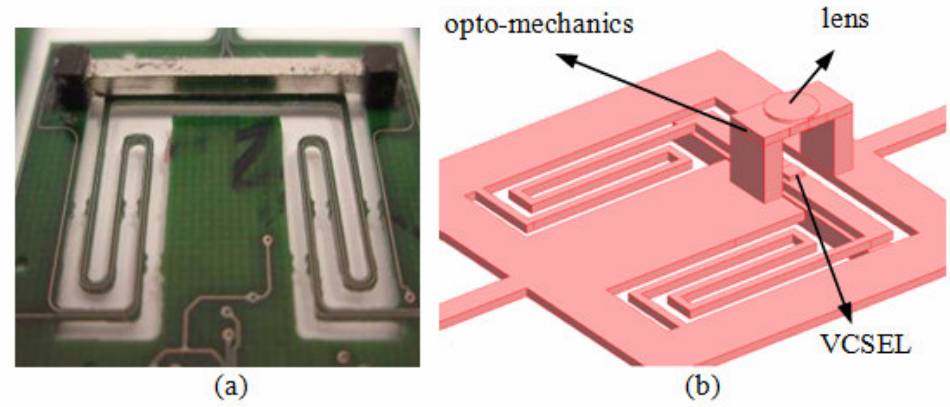


Figure 5-4 (a) Close-up picture of the moving coil laser plunger actuated by an external magnet mounted on the torsional frame underneath the plunger paddle. The magnet is elevated from the surface to leave enough clearance for plunger deflection (bottom view). (b) An illustration of the focusing optics assembly on the FR4 scanner used to focus the laser beam (top view).

### *5.4.2 Experimental Results*

As the torsional scanner is actuated, the laser plunger can be concurrently excited out-of-plane to modulate the beam waist distance. Figure 5-5 shows the AC deflection of the tip of the laser plunger at 10Hz as a function of the drive current through the copper lines routed on its paddle. The nonlinearity in the deflection curve suggests that the drive efficiency is increasing for larger deflections, which is not true for the ideal case. This is actually due to asymmetries in the magnetic circuit due to mounting tolerances and possible

measurement errors of LDV at low frequencies and speeds. The beam waist location is sensitive to tiny deflections of the plunger element due to large magnification. Therefore, accurate DC controllability of this element is essential; thus it is actuated off-resonance.

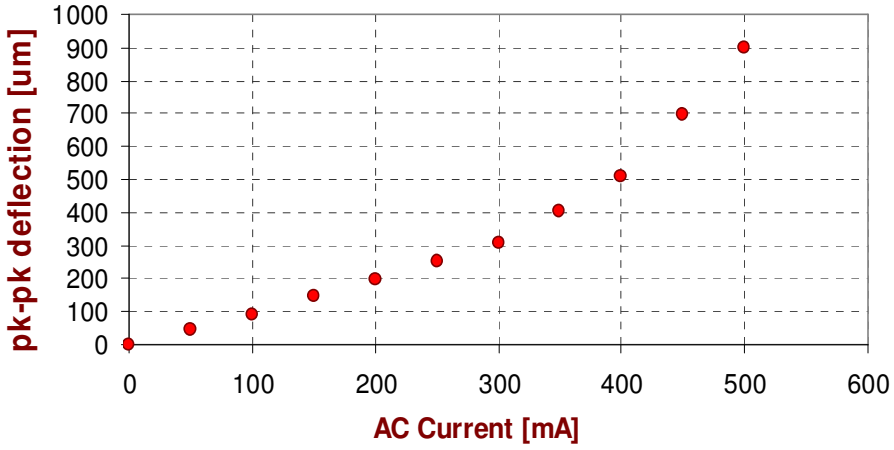


Figure 5-5 Shows the peak-to-peak out-of-plane deflection of laser diode plunger for off-resonant AC actuation at 10Hz. Spring softening observed at higher deflections.

Figure 5-6 shows the experimentally obtained depth of focus curves for the scanning beam. Each curve shows the full-width-at-half-maximum (FWHM) spot size as a function of propagation distance for a different laser diode position with respect to the fixed lens on the scanning frame. The laser diode is displaced a total of 500µm with the plunger actuation, shifting the beam waist location from 80mm to 650mm after the lens. As an example, if the spot size for a barcode reader is 125µm, dynamic focus system allows for extending the depth of focus from 50mm to 250mm. For applications requiring spot size about 500µm, the depth of focus can be increased up to one meter. The plunger can be deflected more to further extend the depth of field. Hence, the dynamic variable focus feature allows the torsional scanner to scan a long range from almost contact up to one meter with the flying spot always in focus.

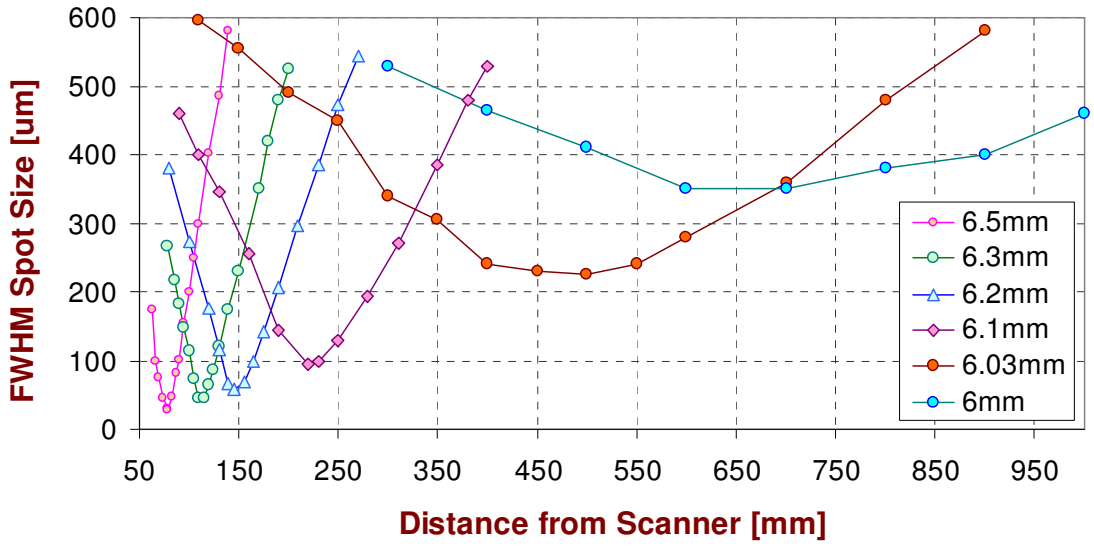


Figure 5-6 Experimental results for the spot size as a function of distance from the scanner. Each curve represents the depth of focus of the beam for a varied laser-to-lens distance as shown in the legend. The total travel range of the VCSEL is about 500µm. (The VCSEL has λ= 672nm, NA= 0.1).

# 6 CONCLUSIONS

This thesis reports the results of design, development, characterization and modeling of FR4 scanners and its integration with optics and optoelectronics. First, FR4 is introduced as a new opto-electro-mechanical systems platform. Then various actuation mechanisms for FR4 scanners are discussed together with detailed discussions on force and deflection calculations. Finally, a novel and high performance FR4 laser scanner with integrated dynamic focusing feature is presented. The scanners can be employed in scan engines for large angle scanning applications such as display and imaging.

FR4 offers a unique platform for millimeter sized opto-electro-mechanical systems. As demonstrated throughout the thesis, low Young's modulus and well-engineered electrical and thermal properties make FR4 very attractive and reliable material particularly for low frequency (< 1kHz) and large deflection scanning applications. In the reliability experiments, FR4 did not show significant fatigue and performance degradation even after operating at large scan angles for several hundred million cycles. No irreversible damage is observed in high temperature tests performed on FR4 scanners. Standard PCB technology can be used to cut the desired shape from a sheet of FR4 with less than 50μm precision. The copper laminates on FR4 can be used for electrical connections and as back-emf position and angles sensor for better control of the scanner. Discrete optical, mechanical and electrical components can be integrated on FR4 scanners.

Three actuation schemes have been discussed: soft magnetic film actuation, moving magnet and moving coil actuation. One of the main contributions of this research is on soft magnetic film actuator modeling. A new technique to calculate magnetic torque for unsaturated magnetic films under nonuniform fields is presented. For dynamic actuation, the magnetic hysteresis is incorporated into the model. The B-H loop of magnetic films is

modeled with a new closed form analytical function. Scaling of the magnetic model to MEMS based systems is also discussed.

A novel FR4 scanner for large angle scanning applications is presented. FR4 and standard PCB technology is used to integrate a two degrees of freedom (DOF) scanner with a VCSEL and focusing optics on the moving platform. 50° scan angle is achieved with resonant magnetic actuation at 60Hz and 500μm peak-to-peak deflection is achieved with off-resonant laser diode plunger on the same platform. The imaging range with 125μm spot size is extended from 50mm to 250mm using a 6mm focal length lens. Imaging from a tilted surface with a dynamically focused spot is also demonstrated enabling advanced imaging applications with depth-scanning capability.

# APPENDIX A: Magnetic Field of Circular and Rectangular Coils

Magnetic field calculation is an important part of magnetic torque modeling. Although finite element modeling tools offer accurate and fast solutions to magnetic field problems, it is important to know the analytical expressions for the magnetic field of different coil geometries. In this section, analytical expressions for calculating the magnetic field of circular and rectangular coils are provided.

## *A.1. Magnetic Field of a Helmholtz Coil*

The on-axis magnetic flux density of a circular coil with air-core is derived from the Biot-Savart law as

$$B = \frac{\mu_0 NIR^2}{2(R^2 + z^2)^{3/2}} \tag{A-1}$$

where N is the total number of turns in the coil, I is the coil current, R is the radius of a single turn and z is the on-axis distance from the coil. The above formula is accurate for thin coils and its accuracy decreases as the coil height increases.

## *A.2. Magnetic Field of a Rectangular Coil*

Magnetic field of a rectangular coil has a more complicated analytical expression compared a circular loop.

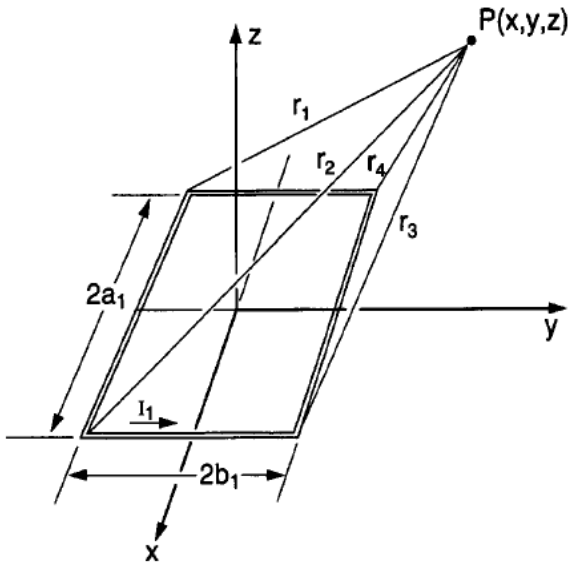


Figure A-1 A rectangular current loop in x-y plane centered about z axis

For a rectangular loop in x-y plane as shown in Figure A–1, z component of magnetic flux density at a point (x,y,z) is given by [39]

$$B_z = \frac{\mu_0 NI}{4\pi} \sum_{a=1}^{4} \frac{(-1)^{\alpha} d_{\alpha}}{r_{\alpha}[r_{\alpha} + (-1)^{\alpha+1} C_{\alpha}]} - \frac{C_{\alpha}}{r_{\alpha}[r_{\alpha} + d_{\alpha}]} \tag{A-2}$$

where $C_{\alpha}$ is given by

$$C_1 = -C_4 = a_1 + x \quad \text{and} \tag{A-3}$$

$$C_2 = -C_3 = a_1 - x$$

and $d_\alpha$ is given by

$$d_1 = d_2 = y + b_1 \quad \text{and} \tag{A-4}$$

$$d_3 = d_4 = y - b_1$$

The distances $r_\alpha$ to the point of observation are given by

$$r_1 = \sqrt{(a_1 + x)^2 + (y + b_1)^2 + z^2}$$

$$r_2 = \sqrt{(a_1 - x)^2 + (y + b_1)^2 + z^2} \tag{A-5}$$

$$r_3 = \sqrt{(a_1 - x)^2 + (y - b_1)^2 + z^2}$$

$$r_4 = \sqrt{(a_1 + x)^2 + (y - b_1)^2 + z^2}$$

The x and y components of the flux densities at a given point (x,y,z) is given by

$$B_x = \frac{\mu_0 NI}{4\pi} \sum_{a=1}^{4} \frac{(-1)^{\alpha+1} z}{r_\alpha [r_\alpha + d_\alpha]} \tag{A-6}$$

$$B_y = \frac{\mu_0 NI}{4\pi} \sum_{a=1}^{4} \frac{(-1)^{\alpha+1} z}{r_\alpha [r_\alpha + (-1)^{\alpha+1} C_\alpha]} \tag{A-7}$$

## APPENDIX B: Comparison of Moving Coil & Moving Magnet Actuators

In this section, two case studies are analyzed for different moving coil and moving magnet actuated scanners. This study mainly aims to investigate which actuation scheme is more power efficient given that the scan engines meet the same resonant frequency specification. In this analysis, the actuators are excited at the same power consumption level, and the scan angles achieved with each design is calculated. The scan angles are calculated for off-resonance actuation, so quality factor variations depending on design are not accounted for.

It is important to note that this comparative analysis does not intend to provide generic rules of scanner design, since each application has a different set of specifications and constraints. Therefore, the conclusions of this study may not apply to all scan engine design problems. There are many other constraints for a product such as cost, form factor, packaging constraints and design rule limitations which have to be added to the design equations. However, even in such cases, this study can provide an insight for magnetic actuator design, especially for the inertia, resonant frequency and power consumption aspects. The study is conducted on FR4 scanners, however the perspective is independent of platform and results are applicable to general magnetic actuator design.

Simple illustrations of magnetic actuators simulated for this case study are given below.

*Moving magnet design:* The external coil of the moving magnet actuator studied here is an air-core coil wrapped with a permeable jacket to increase the flux inside. No permeable core is used inside the coil. The permanent magnet on the scanner platform is

almost embraced by the air-core coil, since highest vertical magnetic field for a coil is achieved inside it. A simple illustration of the magnetic circuit is shown below. The scanner is not shown in Figure B- 1; however in the actual design, the magnet is mounted on the scanner, so that the scanner platform is on top of the coil.

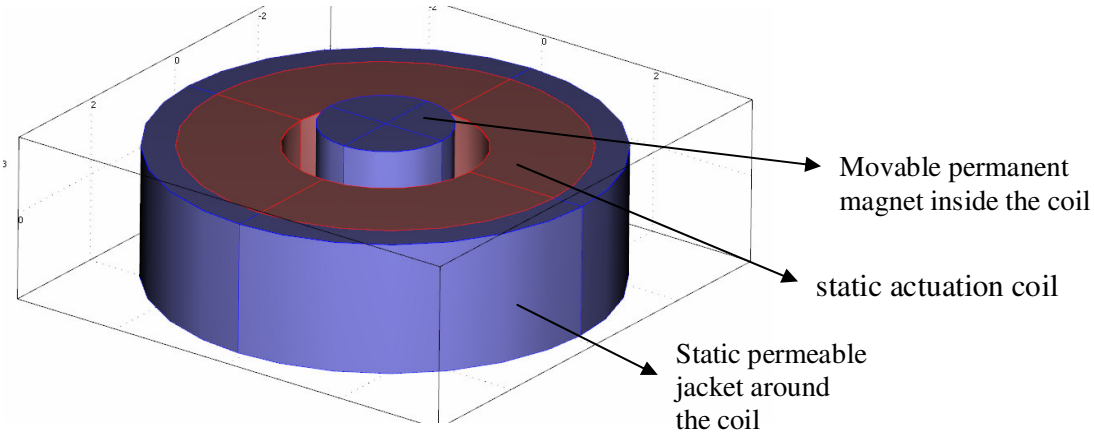


Figure B- 1 Illustrates the basic magnetic circuit used for moving magnet actuator design

The permeable jacket around the coil almost doubles the magnetic field inside the coil (Figure B- 2). Therefore, this magnetic circuit design is chosen for the comparative study of moving magnet and moving coil actuators. FEA analysis of the magnetic circuit is performed for magnetic torque calculations.

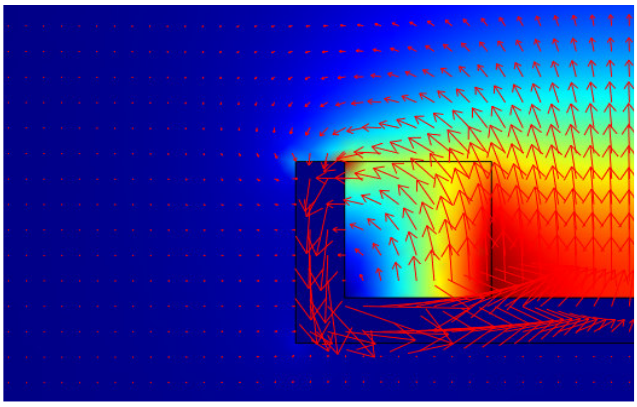

Figure B- 2 Shows a 2D cross-section of the circular coil wrapped with a permeable jacket. The permeable piece around the coil concentrates the magnetic field inside the coil, where the moving magnet is placed.

*Moving coil design (with a discrete coil mounted on scanner):* A discrete coil is mounted on the scanning frame and static magnets and field closers are employed to enhance the magnetic flux density. A basic illustration of the magnetic circuit employed is shown below. FEM analysis of such a magnetic circuit reveals that 0.4T average magnetic flux density along y-direction on the coil can be achieved with a good design.

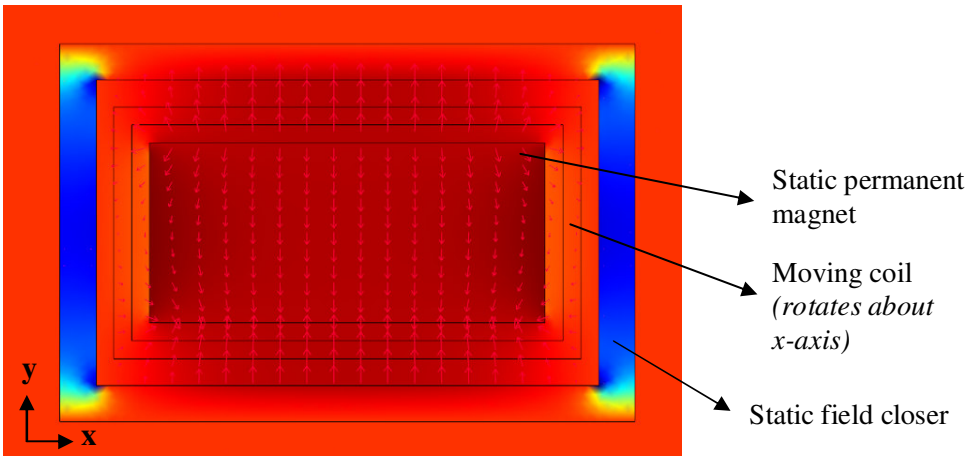


Figure B- 3 Illustrates the Magnetic circuit employed for moving coil scanner, where a discrete coil is mounted on the scanning frame. (scanning frame not shown)

*Moving coil design (planar coil routed on the scanner):* In this design, the coil is routed on the scanner, resulting in a very low inertia actuator. An efficient magnet circuit design allows about 0.4T magnetic flux density on the movable coil. The magnet and field closers are static. An illustration of an efficient magnetic circuit is shown in Figure B- 4.

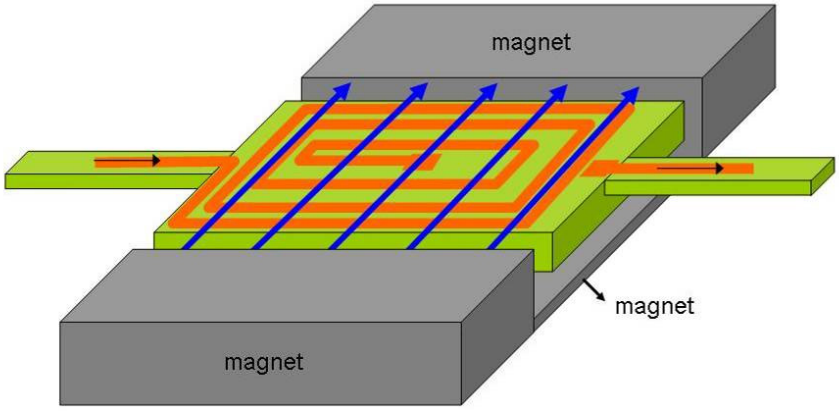


Figure B- 4 Illustrates the magnet circuit for a moving coil scanner, where a planar coil is routed on the scanner

Two cases are studied below. In both cases, the torsion mode frequency is kept the same for all actuation schemes and a magnetic motor is designed to actuate the scanner efficiently. In case 1, spring constants are also kept the same for all actuators, hence the magnetic motors are constrained to have the same inertia. In case 2, spring constants of the scanners are allowed to be different, hence the inertias of the magnetic motors are different.

***Case 1*:** In this case, all scanners are designed to have torsion mode resonance at 1.1 kHz and spring constants of the actuators are kept the same. Therefore, to maintain the same resonant frequency for all scanners, the inertia of the magnetic circuit element

(magnet or coil) on the scanning frame is designed to be equal. Since mechanical designs are the same in this case, the efficiency of the scan engine is dominated by the magnetic motor efficiency.

A review of Table B- 1 shows that there is not a very significant power efficiency difference in the actuator design. The moving coil designs have the same scanning performance at the same power. For planar coil design, the mirror size had to be larger than the discrete coil design, to achieve the inertia needed to bring the resonant frequency down to 1.1 kHz. The moving magnet design provides slightly more scan angle at the same power.

| | **Spring Constant [Nm/rad]** | **Total Inertia [km.m$^2$]** | **Magnetic Torque [Nm]** | **Total Optical Scan Angle [deg]** | **Mirror Size [mm]** |
|---|---|---|---|---|---|
| **Moving magnet** | 1.16e-3 | 2.4e-11 | 8.44e-5 | 17 | 5 |
| **Moving coil** *(discrete coil)* | 1.16e-3 | 2.4e-11 | 6.44e-5 | 13 | 3 |
| **Moving Coil** *(planar coil routed on scanner)* | 1.16e-3 | 2.4e-11 | 6.97e-5 | 13 | 5 |

Table B- 1 Summarizes the actuator design parameters and the scanning performance for different Magnetic actuation schemes. Spring constant and resonant frequency of all actuators are designed to be the same.

***Case 2*:** In this case, all scanners are designed to have torsion mode resonance at 250 Hz and spring constants of the actuators are allowed to vary to optimize the design. Therefore, the inertias of the magnetic circuit element (magnet or coil) on the scanning frame are different.

Table B- 2 reveals that the moving coil actuator with the planar coil is the champion since it provides substantially better scan angle at the same power level.

In general, permanent magnet and moving coil actuators have similar inertia and spring constant values, if the coil is discrete. However, for a planar coil, the inertia of the structure is much lower. As seen in Table B- 2, planar moving coil design has about 65 times less inertia compared to other designs. Therefore, to keep the resonant frequency of the scanner the same, it has 65 times lower spring constant. Although, the planar moving coil design produces much less magnetic torque (10 times less than the moving magnet actuator) due to limited number of coil turns, its low spring constant still gives a much better scanning performance.

| | **Spring Constant [Nm/rad]** | **Total Inertia [km.m$^2$]** | **Magnetic Torque [Nm]** | **Total Optical Scan Angle [deg]** | **Mirror Size [mm]** |
|---|---|---|---|---|---|
| **Moving magnet** | 3.88e-3 | 1.3e-9 | 6.86e-4 | 40 | 5 |
| **Moving coil** *(discrete coil)* | 3.88e-3 | 1.3e-9 | 4.94e-4 | 30 | 5 |
| **Moving Coil** *(planar coil routed on scanner)* | 5.87e-5 | 1.97e-11 | 6.99e-5 | 273 | 5 |

Table B- 2 Summarizes the actuator design parameters and the scanning performance for different magnetic actuation schemes. Resonant frequency of all actuators are designed to be the same, but spring constant is different for each design.

The optimum choice of actuation scheme is actually a much more complicated process than what is discussed in this section. Many other constraints and specifications may dominate the design, necessitating a different design philosophy. However, as a rule of thumb, it can be argued that the lowest inertia design is the most power efficient choice among different magnetic actuators. With low-inertia scanners, low-frequency operation requires low-stiffness flexure design, which makes the flexures susceptible to large deflections and high stress caused by shock and vibration. Therefore, when low-operation frequency is desired, better choice is to use a low-stiffness material, such as FR4, and use moving magnet or moving discrete coil architectures.

## BIBLIOGRAPHY

[1] http://en.wikipedia.org/wiki/Galvanometer

[2] H. Urey, "Retinal Scanning Displays", *Encyc. of Optical Engineering*, Marcel-Dekker, 2003.

[3] P. De Dobbelaere, K. Falta, L. Fan, S. Gloeckner, and S. Patra, "Digital MEMS for Optical Switching", IEEE Communications Magazine, March 2002

[4] D. J. Bishop, C. R. Giles, and G. P. Austin, "The Lucent LambdaRouter: MEMS Technology of the Future Here Today", IEEE Communications Magazine, March 2002

[5] H. Miyajima, K. Murakami, and M. Katashiro "MEMS Optical Scanners for Microscopes" IEEE Journal of Selected Topics in Quantum Electronics, vol. 10, no. 3, May/June 2004

[6] H. Ra, W. Piyawattanametha, Y. Taguchi, D. Lee, M. J. Mandella, and O. Solgaard, "Two-Dimensional MEMS Scanner for Dual-Axes Confocal Microscopy", Journal of Microelectromechanical Systems, vol. 16, no. 4, August 2007

[7] G. J. Tearney, M. E. Brezinski, B. E. Bouma, S. A. Boppart, C. Pitris, J. F. Southern, J. G. Fujimoto "In Vivo Endoscopic Optical Biopsy with Optical Coherence Tomography" *Science* 27 June 1997: Vol. 276. no. 5321, pp. 2037 - 2039

[8] J. M. Schmitt, "Optical Coherence Tomography: A Review", IEEE Journal of Selected Topics in Quantum Electronics, vol. 5, no. 4, July/August 1999

[9] S. Holmstrom, A. D. Yalcinkaya, S. Isikman, C. Ataman, H. Urey, "FR-4 as a New MOEMS Platform", IEEE-LEOS Optical MEMS Conference, p.25-26, Hualien, Taiwan, August 2007

[10] H. Urey, S. Holmstrom, A. D. Yalcinkaya, "Electromagnetically actuated FR4 Scanners", IEEE Photonics Tech. Lett., vol.20, issue 1, p.30-32, 2007

[11] Georgia Institute of Technology "Introduction to Electronic Packaging" course lecture notes. Retrieved from: www.prc.gatech.edu/academics/elpkg/pdf/module3.pdf

[12] http://www.ami.ac.uk/courses/ami4809_pcd/unit_01/index.asp#8

[13] S. Ehrler, "Properties of new printed circuit board base materials", Circuit World, vol.28, iss.4, pg.38-44, 2002

[14] P.F. Van Kesel, L.J. Hornbeck, R.E. Meier, M.R. Douglass, "A MEMS Based Projection Display", Proceedings of the IEEE, vol.86, no.8, 1998

[15] A. D. Yalcinkaya, O. Ergeneman, H Urey, "Polymer Magnetic Scanners for Bar Code Applications," Sensors and Actuators A, Vol. 135, pp. 236-243, 2007

[16] C. Durand, F. Casset, P. Renaux, N. Abelé, B. Legrand, D. Renaud, E. Ollier, P. Ancey, A. M. Ionescu, and L. Buchaillot "In-Plane Silicon-On-Nothing Nanometer-Scale Resonant Suspended Gate MOSFET for In-IC Integration Perspectives", IEEE Electron Device Letters, vol. 29, no. 5, May 2008

[17] Symbol Technologies, "New Technologies Drive Superior Scan Engine Performance", Technical white paper, January 2006. Retrieved from URL: *http://www.motorola.com/staticfiles/Business/Products/Bar Code Scanners/Fixed Mount Scanners/MiniScan 4400/_Documents/Static Files/NewTechnologies.pdf*

[18] S.G. Kelly, "Fundamentals of Mechanical Vibrations" 2nd ed., pg. 252-258, McGraw Hill, 2000

[19] H. Urey, C. Kan and W. Davis, "Vibration mode frequency formulae for micromechanical scanners" Journal of Micromechanics Microengineering, 15, pp. 1713-1721, 2005.

[20] J. Judy, "Batch-Fabricated Ferromagnetic Microactuators with Silicon Flexures", (PhD dissertation, UC Berkeley, 1996), 154-165

[21] S. O. Isikman, O. Ergeneman, A.D. Yalcinkaya, H. Urey, "Modeling and Characterization of Soft Magnetic Film Actuated 2D Scanners," Journal of Selected Topics in Quantum Electronics, Vol. 12, pp.283-289, Mar/Apr. 2007

[22] S. O. Isikman, H. Urey, "Dynamic Modeling of Magnetic Film Actuators", IEEE LEOS Special Symposium on Optical MEMS and NEMS, Orlando, USA, Nov 2007

[23] S.O. Isikman, H. Urey, "Dynamic Modeling of Magnetic Film Actuated Scanners", submitted to IEEE Transactions on Magnetics, 2008

[24] C. Liu and Y.W. Yi "Micromachined magnetic actuators using electroplated permalloy", IEEE Transactions on Magnetics, Vol. 35, Issue 3, pp. 1976-1985, 1999.

[25] J. Judy, R. S. Muller, "Magnetically actuated, addressable microstructures", IEEE/ASME J. MEMS, Vol 6, no. 3, pp 249-256, 1997.

[26] D. Jiles, Introduction to Magnetism and Magnetic Materials, Chapman & Hall, New York, 1991.

[27] E. Erden, E. C. Siringil, S. O. Isikman, H. Urey, "Self-oscillating FR4 Scanner with Closed-loop Control and Fast Start" in preparation for IEEE Sensors and Actuators: A, 2008

[28] J. Moreland, A. Jander, J. Beall, P. Kabos, S. Russek, "Micromechanical torque magnetometer for in situ thin-film measurements", IEEE Transactions on Magnetics, vol.37, no.4, (2001)

[29] O. Cugat, J. Delamare, G. Reyne, "Magnetic micro-actuators and systems (MAGMAS)", IEEE Transactions on Magnetics, vol.39, no.5, (2003)

[30] H. Urey, D. W. Wine, and J. R. Lewis, "Scanner design and resolution tradeoffs for miniature scanning displays," Flat Panel Displays, Proc. SPIE vol. 3636, San Jose, California, January 1999.

[31] B.E.A. Saleh, M.C. Teich, "Fundamentals of Photonics", John Wiley & Sons (1991)

[32] S. Kuiper and B. H. W. Hendriks, App. Phys. Lett., 85, 1128 (2004)

[33] Y. Shao, D.L. Dickensheets, P. Himmer, "3-D MOEMS Mirror for Laser Beam Pointing and Focus Control" IEEE Journal of Selected Topics in Quant. Electronics, vol.10, no.3, May/June 2004

[34] A. Kaplan, N. Friedman, N. Davidson, "Acousto-optic lens with very fast focus scanning" Optics Letters, vol.26, iss.14, 1078-1080

[35] M.Ye, S.Sato, "Liquid crystal lens with focus movable along and off axis" Optics Comm., vol.225, iss.4-6, p. 277-280 (2003)

[36] S. Kwon, V. Milanovic, L.P. Lee, "Large-displacement vertical microlens scanner with low driving voltage", Photonics Technology Letters, vol. 14, iss.11, p. 1572-1574, 2002

[37] S. A. Self, "Focusing of Spherical Gaussian beams," Applied Optics 22, 658- (1983)

[38] S.O. Isikman, R. Sprague, H. Urey, "FR4 Laser Scanner with Dynamic Focus", submitted for publication to Photonics Technology Letters, 2008

[39] M. Misakian, "Equations for the Magnetic Field Produced by One or More Rectangular Loops of Wire in the Same Plane" Journal of Research of the National Institute of Standards and Technology 105, 557 (2000)

# VITA

Serhan O. Isikman was born in Ankara, Turkey in 1983. He received his B.S. degree in Electrical and Electronics Engineering from Koc University in 2006. Same year, he joined Optical Microsystems Laboratory (OML) of Koç University, Department of Electrical Engineering as an M.Sc candidate. He will join the Electrical Engineering department of University of California, *Irvine*, USA to pursue his Ph. D degree in the field of photonics in 2008.

Serhan Isikman is a student member of IEEE and IEEE-LEOS.